Research Square

Preprints are preliminary reports that have not undergone peer review.
They should not be considered conclusive, used to inform clinical practice,
or referenced by the media as validated information.

Tuning Costimulatory Signaling and Activation Domains in TCR-Like Chimeric Antigen Receptors to Optimize Functional Avidity at Low Antigen-Density Thresholds

Ofir Levin-Piaeda
Technion-Israel Institute of Technology
Noam Carmi
Technion-Israel Institute of Technology
Carmel Sochen
Weizmann Institute of Science
Moshe Biton
Weizmann Institute of Science
Maya Cohen
Technion-Israel Institute of Technology
Yoram Reiter
reiter@technion.ac.il

Technion-Israel Institute of Technology

Research Article

Keywords: TCR-like CAR, Functional Avidity, Costimulatory Domains

Posted Date: November 17th, 2026

DOI: https://doi.org/10.21203/rs.3.rs-11512240/v1

License: This work is licensed under a Creative Commons Attribution 4.0 International License.
Read Full License

Additional Declarations: No competing interests reported.

Tuning Costimulatory Signaling and Activation Domains in TCR-Like Chimeric Antigen Receptors to Optimize Functional Avidity at Low Antigen-Density Thresholds

Ofir Levin-Piaeda, Noam Carmi, Carmel Sochen[#], Moshe Biton[#], Maya Cohen and Yoram Reiter*

Laboratory of Molecular Immunology and Immunotherapy, Faculty of Biology,

Technion-Israel Institute of Technology, Haifa 3200003, Israel

Department of Immunology and Regenerative Biology, Weizmann Institute of Science, Rehovot 7610001, Israel

*Corresponding author: reiter@technion.ac.il

Key words: TCR-like CAR, Functional Avidity, Costimulatory Domains

Footnotes: Manuscript was edited using the AI software ChatGPT. Figure 1A was generated using Bio render software

Conflict of Interest statement: The authors declare no conflict of interest

Acknowledgments: RNAseq and its data analysis was performed in collaboration with The Mantoux Bioinformatics institute of the Nancy and Stephen Grand Israel National Center for Personalized Medicine, Weizmann Institute of Science, Rehovot, Israel

Abstract

Chimeric antigen receptor (CAR) T-cell therapy has demonstrated remarkable efficacy in hematological malignancies, yet its translation to solid tumors remains limited by heterogeneous and often low target antigen density. TCR-like (TCRL) based CARs, which recognize intracellular antigens presented by major histocompatibility complex (MHC) molecules, significantly expand the targetable landscape for solid tumors such as melanoma.

In this study, we systematically investigated how the integration of distinct costimulatory domains (CD28 and 4-1BB) and primary activation elements (CD3ζ versus FcRγ) dictates the functional avidity outcome of TCRL CAR T-cells targeting the melanoma-associated Tyrosinase/HLA-A2 complex. Using a well-defined experimental system with controlled antigen densities, we profiled the phenotypic, cytolytic, and transcriptomic landscapes of multiple second- and third-generation CAR architectures.

Our results demonstrate that CD28-based signaling lowers the antigen density threshold required for robust immediate cytotoxicity but renders the T-cells susceptible to rapid exhaustion upon chronic stimulation. In contrast, 4-1BB costimulation confers a distinct transcriptomic fingerprint that limits exhaustion, albeit requiring higher antigen density for optimal initial activation. Crucially, structural tuning of these modules led to the engineering of a novel hybrid CAR construct that integrates both CD3ζ and FcRγ activation domains in a position-dependent manner. This novel hybrid configuration exhibited synergistic signal amplification, overcoming the low-antigen-density barrier and demonstrating superior functional sensitivity in our in vitro models. Together, these exploratory findings elucidate the critical interplay between biophysical binding properties, costimulatory signaling, and primary activation elements, providing a strong rational framework for future in vivo evaluation of optimized TCRL-based CAR T-cell therapies.

Introduction

Cancer-specific adoptive immunotherapy, particularly utilizing chimeric antigen receptor (CAR) engineered T-cells, has revolutionized the treatment paradigm for hematological malignancies, yielding durable clinical responses [1], [2]. However, translating this success to solid tumors remains a formidable challenge. A primary hurdle is the paucity of highly specific surface antigens, compounded by the immunosuppressive tumor microenvironment and pronounced antigen heterogeneity [3]. To broaden the applicability of CAR T-cell therapy, TCR-like (TCRL) CARs have been developed. These receptors combine the potent, MHC-independent signaling machinery of classical CARs with the fine specificity of a T-cell receptor (TCR), enabling the targeting of intracellular tumor-associated antigens presented as peptides on MHC molecules [4], [5]. For instance, the melanoma-associated antigen Tyrosinase, presented by HLA-A2, serves as an optimal target for directing highly specific anti-tumor responses [6].

Despite the expansion of the targetable antigen pool, the efficacy of CAR T-cells in solid tumors is heavily dictated by the biophysical properties of the immune synapse, particularly the target antigen density. Solid tumors frequently downregulate antigen expression as a mechanism of immune evasion, dropping below the critical threshold required for robust CAR T-cell activation [7]. Recent studies have highlighted that insufficient reactivity against target cells with low antigen density is a primary driver of CAR T-cell resistance and relapse [8]. Greenman et al., have previously demonstrated that the functional avidity of CAR T-cells is governed by an intricate, non-monotonic interplay between receptor affinity, avidity, and antigen density, where phenomena such as CAR downmodulation play a pivotal regulatory role in preventing overactivation and exhaustion [9], [10].

A critical determinant of the antigen density threshold and subsequent T-cell fate is the intracellular signaling architecture incorporated into the CAR. While the roles of costimulatory endodomains—such as CD28 (associated with rapid, intense effector functions but metabolic exhaustion) and 4-1BB (associated with slower onset, oxidative phosphorylation, and enhanced persistence)—are well-documented [11], [12], [13], [14], the primary activation domains (Signal 1) are less frequently optimized.

Traditional CARs rely almost exclusively on the CD3ζ chain; however, alternative immunoreceptor tyrosine-based activation motif (ITAM)-containing elements, such as FcRγ, offer distinct signaling kinetics and intensities. Furthermore, the spatial arrangement and synergistic potential of combining these distinct activation modules within advanced CAR architectures remain largely underexplored.

In this study, we aimed to bridge this knowledge gap by systematically defining the optimal combinatorial design of both costimulatory and activation elements for TCRL-based CAR T-cells targeting Tyrosinase/HLA-A2. We engineered a diverse library of second- and third-generation CAR architectures, strictly controlling the gradient of target antigen densities. Most notably, we introduce a novel hybrid CAR configuration that physically integrates multiple activation elements (CD3ζ and FcRγ) alongside costimulation. By evaluating their functional output and mapping their activation, exhaustion, and transcriptomic trajectories, our findings reveal construct-specific fingerprints and highlight the superior signal amplification of this novel hybrid design. This in vitro study explores the critical signaling thresholds required to balance immediate cytolytic potency with early indicators of functional durability, ultimately providing an exploratory blueprint for the next generation of rationally designed CAR T-cells targeting solid tumors and/or hematological malignancies

Materials and Methods

Cell growth

Human tumor cell lines used in this study included HLA-A2-positive/Tyrosinase positive melanoma cell lines: 526, SKMEL23 and 501.A. 1938 human tumor melanoma cells, which lack endogenous expression of tyrosinase but consist of HLA-A2 expression, were used as a negative control. Unless otherwise mentioned, cells were cultured in RPMI-1640 medium containing 10% fetal bovine serum (FBS), 100 units/mL penicillin, 100 mg/mL streptomycin, 0.5 mmol/L HEPES, 1 mmol/L sodium pyruvate, nonessential amino acids, and 2 mmol/L glutamine at 37°C in 5% CO2. Peripheral blood mononuclear cells (PBMCs), and T cells were cultured in T-cell culture medium (T cells CM), which was additionally supplemented with 0.05 mmol/L 2-mercaptoethanol and the described units of IL2 at 37°C in 5% CO2. The HEK293 Phoenix-Ampho cells were maintained in Dulbecco's modified Eagle's medium and with 10% FBS, 100 units/mL penicillin, 100 mg/mL streptomycin, 0.5 mmol/L HEPES, 1 mmol/L sodium pyruvate, nonessential amino acids, and 2 mmol/L glutamine at 37°C in 5% CO2.

Reagents and antibodies

Unless otherwise mentioned, all media and cell growth reagents were purchased from Thermo Fisher Scientific. Oligonucleotides were manufactured at HPLC quality by Sigma Aldrich (Merch). All restriction enzymes were purchased from NEB. The following commercial antibodies were used in this work: PE conjugated anti-mouse Ig Kappa light chain (clone RMK-45, RRID: AB_2563580, BioLegend), PE conjugated goat anti-mouse IgG (AB_315010, BioLegend), Alexa Fluor 647 conjugated goat anti-mouse IgG $F(ab')_2$ fragment specific (RRID: AB_2338910, Jackson), anti-CD8 (RRID:AB_2075388, BioLegend), anti-CD4 (RRID:AB_395752, BD Biosciences), CD25 (RRID:AB_1257140, Thermo Fisher Scientific), CD137 (4-1BB) (RRID: AB_830672, BioLegend), anti-CTLA4 (RRID: AB_10805626, eBioscience), anti–PD-1 (CD279) (RRID:AB_2562256, BioLegend), anti–LAG-3 (CD223) (RRID:AB_2632951, BioLegend) and anti–TIM-3 (CD366) (RRID:AB_2565833, BioLegend). Isotype controls were included where indicated.

Control A2-Tyr Antigen Density

For experiments controlling A2-Tyr antigen density within the target system, surface A2-Tyr levels were assessed on the day of the experiment by flow cytometry using the TCR-like antibody (clone Fab-D11), developed and characterized in our laboratory [10], and those cells were used immediately for functional assays. By using the QuantiBRITE PE kit (RRID:AB_2868736, BD Biosciences) calibration beads, we created a calibration curve of PE mean fluorescence intensities (MFI) for 0–10000 PE molecules for each cytometer setting, and through the use of such a calibration curve we were able to convert each MFI resulting from the binding of our TCR-like Abs into a number of PE molecules that directly correlates to the number of HLA-A2-peptide complexes detected by the TCR-like Ab. These data represent the number of sites per cell [15]

Purification of Fab fragments

Fab-D11 clone was expressed by transfection of the heavy-chain and light-chain constructs to Expi293 cells (Cat# A41249, Thermo Fisher Scientific) according to the manufacturer's protocol. Aliquots were kept in -80^{0}C.

CARs Constructs Design, Cloning and Expression

For generating a chimeric receptor, anti-Tyr TCR-like Fab TA2 was converted to scFv forms by connecting the carboxyl-terminus of the VL region and the amino-terminus of the VH region by a peptide linker as described previously [9] . DNA constructs were ordered from GeneArt, Thermo Fisher Scientific. The scFv was connected via the carboxyl-terminus of the VH region to a CD28–hinge chain. The 8 different second and third generation CAR constructs were generated to enable direct comparison of CAR T cells targeting a peptide–MHC complex. A2-Tyr–targeting CARs were designed with an identical scFV CAR backbone comprising an scFv fused to CD28-hinge-TM and variable co-stimulatory-activatory signaling domains, linked to 2A self-cleaving peptides followed by GFP. A2-Tyr CAR incorporated a TCR-like scFv recognizing the HLA-A2–restricted tyrosinase peptide, previously characterized in our laboratory and based on a TCR-like binding format described by Greenman et al [10]. All constructs were modularly cloned into the pBullet retroviral vector (RRID:Addgene_53067) using the EcoRI and BamHI restriction enzymes,

enabling co-expression of CAR and fluorescent reporter, and were sequence-verified prior to use. Retroviral vectors were produced by transient transfection of Phoenix-Ampho packaging cells with CAR constructs together with Gag–Pol and GalV envelope plasmids, and viral supernatants were harvested 48 h post-transfection for T cell transduction. To normalize CAR expression levels between 8 different A2-Tyr–CAR constructs, GFP-positive cells were enriched by flow-cytometric sorting (BD FACSAria-IIIu OR Invitrogen Bigfoot cell sorter). Sorting gates were adjusted to match median GFP fluorescence intensity between populations prior to functional assays. GFP was used as a surrogate for CAR expressions because all constructs were encoded in a pBullet-2AP GFP vector, linking GFP expression to CAR transcription. For avidity measurements and CARs surface expression correlated to endogenies GFP, cells were incubated with a conjugated commercial antibody APC Goat anti-Mouse IgG, $F(ab')_2$ fragment specific (Jackson). Following washing, cells were analyzed at the Calibur flow cytometer (BD Biosciences). Functional measurements of avidity-sorted CAR T cells were performed 2 days after sorting.

Transduction of retroviral CAR constructs into primary human T cells, activation and expansion

Retroviral transduction was performed on primary T cells, using the Phoenix amphotropic packaging cells, as described previously. Briefly, $2X10^6$ Phoenix amphotropic packaging cells were cultured in 10-cm culture plated for 24 hours at 37^0C with 5% CO2. The cells were transfected with the vector constructs along with Gag-Pol and envelope GalV constructs, using calcium phosphate transfection precipitation kit (Invitrogen Thermo Fisher Scientific) according to the manufacturer's protocol. After culturing for 48 hours and replacing medium, the viral supernatants were harvested. PBMCs were isolated from healthy male and female donors under Technion Helsinki Committee approval, using density gradient centrifugation according to the Ficoll-Paque technique. PBMCs were activated 72 hours prior to transduction using the anti-CD3 (Clone: OKT3, RRID: AB_468854) and soluble anti-CD28 antibodies at 30 ng/Ml (RRID:AB_396492) and human IL2 (600 U/mL). For retroviral transductions, retronectincoated (Takara) untreated 24-well plates were seeded with the viral supernatant, centrifuged for 30 minutes, according to the manufacturer's protocol. PBMCs were then added at $1X10^6$ cells per 1 mL. After 24

hours at 37^{o}C with 5% CO2, half the culture medium was replaced with fresh medium. After further 48-hour culture period, flow cytometry analysis was performed by a Calibur flow cytometer (BD Biosciences) to determine transduction efficiency. Five days after transduction, cells were collected, washed, and stained with anti-CD8 antigen presenting cells (APCs) with PBS/ 0.5%BSA buffer. After wash, GFP positive PBMCs were sorted by an AriaIII flow cytometer (BD Biosciences). After 3 days, cells went a rapid expansion protocol (REP) as described previously [16]. Briefly, 1.5-2x10^{5} sorted PBMCs were added to upright T-25 flasks containing 30 ng/mL OKT3 (eBioscience), 3,000 U/mL IL2, and 2x10^{8} allogeneic irradiated (50 Gy) PBMC feeder cells obtained by pooling PBMC from normal donors (obtained from the Blood Bank) in 1:1 mixture of complete RPMI and AIM-V medium. On day 5, 10 mL of the medium was replaced by fresh AIM V medium with 3,000 U/mL IL2 (final concentration). The CAR T cells were expanded until day 14 and diluted as needed with periodic medium replacement and IL-2 supplementation (1,000 IU/mL) (Cat# 200-02, PeproTech) to keep the viable cell at density of 1-2X10^{6}/mL. Expanded CAR T cells were harvested and cryopreserved in liquid nitrogen for subsequent experiments.

General Flow Cytometry Methods

Flow cytometry was used to assess antigen expression, CAR expression and T-cell activation. Data were acquired on FACSCalibur or Cytek Aurora – Spectral analyzer flow cytometers and analyzed using FlowJo software (RRID:SCR_008520, BD Biosciences). Cell sorting was performed on a FACSAria IIIu (BD Biosciences) or Bigfoot cell-sorter (Invitrogen). For surface staining, cells were incubated with antibodies in PBS containing 0.1% BSA. A2-Tyr was detected using the TCR-like monoclonal antibody FAB-D11, developed and characterized in our laboratory, followed by PE-conjugated goat anti-mouse IgG (eBioscience). CAR expression was monitored by GFP fluorescence, and T cells were identified using anti human CD4 antibody (BioLegend) and anti human CD8 (BD Biosciences). Isotype controls were included where indicated. T-cell activation was assessed by staining for CD25 and CD137 (4-1BB) (BioLegend). anti-CTLA4 (eBioscience), anti–PD-1 (eBioscience), anti–LAG-3 (CD223) (eBioscience) and anti–TIM-3 (CD366) (eBioscience).

In Vitro Functional Assays

LDH Cytotoxicity Assays

CAR T-cell cytotoxicity was measured using a commercially available LDH Non-Radiactive Cytotoxicity Assay (Promega) according to the manufacturer's instructions. Target melanoma cell lines 1938, 526, SkMEL23 and 501A ($2x10^4$ cells/well) were co-incubated with CAR-positive T cells at E:T ratios of 10:1 to 1:1 for 4 h at 37°C, and absorbance was measured at 490 nm. Specific cytotoxicity was calculated after subtraction of effector and target spontaneous release controls. The percent specific cytotoxicity was calculated as follows:

$$\%Specific\ killing = 100 \times \frac{[Experimental\ value - Effector\ spontaneous\ control - Target\ spontaneous\ control]}{[Target\ maximum\ control - Target\ spontaneous\ control]}$$

T-Cell Activation and Inhibition Functional Readouts

CAR T-cell activation was assessed by analysis of surface activation markers, cytokine production, intracellular cytokine accumulation, and degranulation following co-culture with target cells. For activation marker analysis, CAR T cells were co-cultured with target cells at an effector-to-target (E:T) ratio of 1:1. Surface expression of CD25, 4-1BB (CD137), PD-1, LAG-3, TIM-3 and CTLA-4 were assessed after 20–24 h by flow cytometry. For cytokine secretion, CAR T cells were co-cultured with target cells at an E:T ratio of 1:1 for 20–24 h, the TNF-α (RRID:AB_468490, BioLegend) and IFN-γ (RRID:AB_315223, eBioscience) levels in cell-free supernatants were quantified by sandwich ELISA using recombinant cytokine standards.

Transcriptional Assay

Smart-seq2 bulk RNA-seq libraries

Libraries were prepared using a modified SMART-Seq2 protocol [17]. In brief, RNA lysate clean-up was performed using RNAClean XP beads (Agencourt), followed by reverse transcription with Maxima Reverse Transcriptase (Life Technologies) and whole-transcription amplification with KAPA HotStart HIFI 2 × ReadyMix (Kapa Biosystems) for 18 cycles. whole-transcription amplification products were purified with Ampure XP beads (Beckman Coulter), quantified with Qubit dsDNA HS Assay Kit

(ThermoFisher) and assessed with a high-sensitivity DNA chip (Agilent). RNA-seq libraries were constructed from purified whole-transcription amplification products using our in-house Tn5 transposase [18]. The libraries were sequenced on an Illumina Novaseq X. The output was ~20 million reads per sample.

Bioinformatics

Poly-A/T stretches and Illumina adapters were trimmed from the reads using cutadapt; resulting reads shorter than 30bp were discarded. Reads were mapped to the H. sapiens reference genome GRCh38_p13 using STAR (RRID:SCR_004463) [19], supplied with gene annotations downloaded from Ensembl (RRID:SCR_002344) (and with EndToEnd option and out Filter Mismatch Nover Lmax was set to 0.04). Reads with the same UMI were removed using the PICARD Mark Duplicate tool using the BARCODE_TAG parameter. Expression levels for each gene were quantified using htseq-count [20], using the gtf above. Differentially expressed genes were identified using DESeq2 [21] with the beta Prior, cooks Cutoff and independent Filtering parameters set to False. Raw P values were adjusted for multiple testing using the procedure of Benjamini and Hochberg. Pipeline was run using snakemake [22].

Volcano plot

For the bulk RNA-seq analysis, we started from differential expression tables that contained, for each gene, the $\log_2$ fold-change (FC) and false discovery rate (FDR) adjusted p-value for the comparison between T cells alone and T cells co-cultured with the 526 target, separately for each CAR. For every sheet, we selected only the relevant comparison (T-only vs. 526) and removed entries. We then generated a volcano plot, placing the $\log_2$ fold-change on the x-axis and $-\log_{10}$ (adjusted p-value) on the y-axis. Genes were classified as significantly up-regulated or down-regulated using thresholds of $|\log_2 \text{fold-change}| \geq 1.5$ and adjusted p-value ≤ 0.05. Vertical and horizontal dashed lines marked the fold-change and significance cutoffs and top up/down regulated genes are marked.

Experimental data analysis

For Bar-Plots Statistical analyses were performed using GraphPad Prism (RRID:SCR_002798). Data are presented as mean ± SEM unless otherwise indicated. Statistical significance was assessed using one- or two-way ANOVA. For two-way ANOVA, the independent variables (factors) included the specific CAR construct and the target cell line (antigen density), followed by appropriate post hoc multiple-comparison tests as specified in the figure legends. A P value < 0.05 was considered statistically significant. No statistical methods were used to predetermine sample size; group sizes were chosen based on standard practices in similar in vitro preliminary studies. Allocation of samples to experimental groups was not randomized. Investigators were not blinded to group allocation during the experiments and outcome assessment. In all functional assays and figure legends, N represents the number of independent biological donors used to generate CAR T-cells, while n represents the total number of technical replicates evaluated across all independent experiments.

Data extraction from Prism files

Experimental readouts were initially stored as GraphPad Prism XML files (.pzfx). To make the data easier to inspect and process, we converted all Prism files in the analysis folder into standard Excel spreadsheets (.xlsx). For each .pzfx file, all tables contained in the file were automatically read and exported as separate sheets within a single Excel workbook. Before writing the tables to Excel, each table's row index was made explicit as a dedicated "Row" column so that the original row order and identifiers were preserved in the exported files.

Combining multiple experiment files into a single dataset

After converting the raw GraphPad Prism files to Excel, we combined the information from multiple plates/files into a single table for each assay type (e.g., markers, TNF-α and IFN-γ). Each Excel file represents one experiment or plate and contains one or more sheets with measurement values. The goal of this step was to create one unified table per assay, where each row corresponds to a biological condition (e.g., a specific CAT construct and target antigen), and each column corresponds to a readout from one of the experimental runs. For marker panels (classification set to "MARKERS"), we

first grouped all Excel files by sheet name (for example, each marker's data stored in a separate sheet). For each sheet, we merged the corresponding tables from all files based on a shared "Row" identifier, which encodes the experimental condition. When a particular condition was missing in some files, the missing values were filled with zero so that all conditions would be represented across the combined dataset. After merging, missing values were again set to zero, column names were cleaned, and the final combined table for each cytokine was exported as a .csv file for downstream analysis.

Processing and Analysis Pipeline

Final Heat-Map

For each functional assay, we first loaded the processed data table and removed rows including "T only," "1938 N.C," "No Target," and internal technical labels such as "Target". Numerical zeros and empty entries, which represent missing or invalid measurements, were also excluded. Because different assays operate on different numerical scales, each dataset was then normalized independently using a two-step procedure:

1) We computed a global z-score using only non-mock samples to place all assays on a comparable activation scale.
2) We subtracted the mock baseline for each target so that a value of zero represented background activity.

After normalization, all datasets were reshaped into a unified long format and visualized using a strip-plot (a scatter plot with jitter), where each point corresponds to a single measurement, the color denotes the cell type, and the marker shape identifies the assay**.** To evaluate functional specificity, we combined all normalized datasets and analyzed each CAR–target pair. Outliers were removed using a median absolute deviation (MAD)–based filter. Group normality was assessed with the Shapiro–Wilk test, and statistical comparisons were chosen accordingly: normally distributed groups were evaluated using Welch's t-test (which does not assume equal variances), whereas non-normal groups were evaluated using the Mann–Whitney U test. Multiple comparisons were corrected with the Benjamini–Hochberg FDR method, and only combinations whose mean normalized activation exceeded the

mock baseline were considered biologically meaningful. The resulting adjusted p-values were summarized in a heatmap, highlighting which CAR types demonstrated significantly elevated activity toward each target.

Data Availability

All data generated or analyzed during this study are included in the published article and its supplementary information files. Additional information is available from the corresponding author upon reasonable request.

Results

Development of an Integrated Biophysical System for the Characterization of TCR-Like Chimeric Antigen Receptor Architectures

The functional efficacy of CAR-T cells is dictated by a complex interplay of biophysical parameters, primarily binding affinity, avidity, and target antigen density [9], [10], [23]. To rigorously dissect the impact of intracellular signaling domains on T cell fate without the confounding variables of receptor kinetics, we established a highly controlled experimental system (Fig. 1A). Our model utilizes a TCR-like (TCRL) CAR specific for the melanoma-associated Tyr369-377/HLA-A2 complex. Based on prior optimization establishing a non-monotonic relationship between affinity and function [4], [10] we locked the single-chain variable fragment (scFv) affinity at an empirically defined 'Medium' optimum (KD ~ 35nM). We modularly engineered a library of gammaretroviral vectors harboring 8 diverse signaling architectures: single costimulation (CD28 or 4-1BB; 2nd generation), dual costimulation (3rd generation), and distinct activation domains (CD3ζ or FcRγ) (Fig. 1B, 1C).

Primary human T cells were retrovirally transduced, and successful transfection was validated via the level of CAR expression on the surface of cells together with the GFP positive cells. (Fig. 1D). To normalize avidity, these cells were subsequently sorted via fluorescence-activated cell sorting (FACS) to match GFP expression, ensuring overlapping surface receptor densities across all cohorts. Furthermore, to interrogate these architectures under physiological constraints, we utilized a panel of natural HLA-

A2+ melanoma cell lines with quantified, graduated levels of endogenous Tyr-A2 presentation: 1938 (negative), 526 (Low), SKmel (Medium), and 501.A (High) (Fig. 1E). This stringent control ensures that subsequent phenotypic and transcriptomic variations are intrinsically driven by the intracellular signaling engine.

Functional Profiling of Second-Generation TCRL-based CARs Identifies Absolute Dependence on CD3ζ for Primary Cytolysis

Utilizing the calibrated melanoma panel, we first evaluated the functional hierarchy of 2nd-generation constructs. Cytotoxicity was assessed via LDH release assays after 4-hour of co-culture at 10:1 effector-to-target (E:T) ratio (Fig. 2A). To assess T cell activation, we measured T cell surface activation markers CD25 and 4-1BB which are known as late-stage activation markers and evaluated their expression after 20 hours of co-culture. Activation markers **CD25 and 41BB** are significantly upregulated in 28ζ and BBζ constructs (Fig. 2B, 2C).

Beyond cytotoxicity, specific costimulatory domains shaped the activation kinetics. CD28-equipped CARs (28ζ) drove a rapid and potent pro-inflammatory cytokine burst **IFN-γ and TNF-α** (Fig. 2D, 2E). Conversely, 4-1BB (BBζ) induced a more modulated initial response but maintained steady activation marker expression over time, consistent with its known role in ameliorating rapid exhaustion [11], [24]

Indeed, specific evaluation of co-inhibitory markers revealed that the CD28-CD3ζ (28ζ) construct drives a significantly higher accumulation of exhaustion markers, including CTLA-4 and LAG-3, compared to the 4-1BB-CD3ζ (BBζ) construct, further confirming the propensity of CD28 for rapid terminal differentiation (Supplementary Figure S1).

The data revealed an unequivocal requirement for the CD3ζ activation domain (28ζ and BBζ) to execute robust, antigen-specific lysis across all densities (Fig. 2F). Strikingly, architectures relying solely on the FcRγ activation motif (28γ and BBγ) failed to elicit significant target cell death, even at high antigen densities (501.A cells),

indicating that the single ITAM of FcRγ is insufficient to cross the threshold for primary cytolysis.

Third-Generation TCRL-based CARs Architectures Overcome Low-Antigen Density Barriers via Signal Synergy

Solid tumors frequently evade immune surveillance through antigen downregulation. To address this, we hypothesized that increasing intracellular signaling complexity would lower the activation threshold [25], [26]To investigate how dual signaling domain and their position influences CAR T cell functional sensitivity across different antigen densities, we optimized 3rd generation TCRL-based CARs. Our findings highlight that integrating dual co-stimulation (28BBζ) or dual activation domains (28ζγ) maintains high efficacy at Medium-High antigen densities. Cytotoxicity assay demonstrated that the integration of dual costimulation (CD28 + 4-1BB) or synergistic activation domains (CD3ζ + FcRγ) resulted in a profound enhancement of specific lysis (Fig. 3A). Notably, the position-dependent synergy in 28ζγ vs 28γζ highlights that C-terminal FcRγ provides better signal amplification than when placed proximally, especially observed at high antigen densities (Fig. 3B).

This spatial constraint was rigorously validated by comparing the C-terminal FcRγ placement (CD28-CD3ζ-FcRγ) with its proximal counterpart (CD28-FcRγ-CD3ζ), where the distal placement yielded superior cytolytic function. Furthermore, substituting CD3ζ entirely with FcRγ in a dual-costimulation architecture (CD28-41BB-FcRγ) completely abrogated cytotoxicity, reiterating the indispensability of the CD3ζ multi-ITAM core even when supported by dual costimulation (Supplementary Figure S2).

Next, when we added the cytotoxicity assays results together with IFN-γ and TNF-α cytokine secretion, the trend still emphasized on these advanced architectures which maintained robust efficacy even against the 'Low' (526) and 'Medium' (SKmel23) antigen density targets (Fig. 3C, 3D). All functional assays of 3rd generation TCRL-based CARs were normalized and reshaped into a unified format and visualized the readouts on a scatter plot with jitter in parallel to a global computed Z-score indicate distribution of the experimental population (Fig. 3E).

Multiparametric Normalization Identifies Lead Candidates Exhibiting Enhanced Effector Function and Delayed Accumulation of Exhaustion Markers

Together, these results indicate functional outputs of 2nd and 3rd generation CAR T cells. Starting with cytotoxicity, we created functional comparison of 2nd and 3rd generation– TCRL-based CAR T cells across natural melanoma cell lines. Cytotoxicity was assessed via LDH release assays after a 4-hour co-culture at varying effector-to-target (E:T) ratios (Fig. 4A), with optimal functional sensitivity observed at an E:T ratio of 10:1.

To rigorously delineate the optimal signaling architecture, we executed a multiparametric analysis. Recognizing that assays operate on distinct numerical scales, we employed a strict normalization strategy. A global Z-score was computed to establish a unified activation metric. This competitive analysis screening identified 28BBζ and 28ζγ as the lead candidates (Fig. 4B). The 28ζγ construct demonstrated exceptional peak cytolytic potency, while 28BBζ exhibited a highly balanced and sustained effector response. Notably, combined cytokine secretion (IFN-γ + TNF-α) followed a bell-shaped distribution relative to antigen density, peaking at medium densities (Fig. 4C).

The superiority of the lead candidates was firmly established in their regulatory phenotypes: they achieved significant upregulation of late-stage activation markers (CD25, 4-1BB) (Fig. 4D). Cytotoxicity assay also demonstrated the same tendency of the lead candidates (Fig. 4E), while concurrently showing a delayed accumulation of co-inhibitory receptors (PD-1, CTLA-4, LAG-3, TIM-3) typically associated with activation-induced exhaustion [27], [28] (Fig. 4F). This indicates an initial resistance to exhaustion-associated pathways during acute stimulation, providing a basis for future studies on long-term persistence.

Transcriptomic Profiling Unveils Unique Molecular Pathways Associated with Lead Architectures

To elucidate the mechanistic foundations of the distinct functional phenotypes and to dynamically capture the activation-induced transcriptional programming triggered directly during active immune synapse formation, we performed bulk RNA-seq (~20 million reads/sample) on co-cultures representing a mixture of TCRL-based CAR-T cells and low-density 526 melanoma targets. Principal Component Analysis (PCA) plots demonstrated that substituting intracellular domains fundamentally rewires the global genetic program. The samples representing a single cell type form distinct and well-separated clusters—specifically, the T-only, 1938-only, and 526-only samples each cluster independently. (Figure 5A). This is an expected outcome, as distinct cell types are anticipated to exhibit unique expression profiles. Samples containing combinations of these cell types are expected to fall between the single-cell-type clusters, depending on their composition. (Figure 5B). This pattern is clearly observable in the PCA. According to the results observed at the in-vitro assays, the CARs arranged in a manner that supports the correlation according to their functionality.

Transcriptomic profiling of the distinct TCRL-based CAR constructs revealed that the intracellular signaling domains dictate fundamentally dominant immunological different functional pathways upon antigen encounter (Figure 5C). The second-generation CD28-CD3ζ construct exhibited a highly potent pro-inflammatory signature, dominated by the upregulation of cytokines and chemokines (e.g., CCL2, CXCL10). This "effector drive" yields rapid cytotoxicity but poses a high risk for early exhaustion. In contrast, the integration of the FcRγ activation domain with CD28 shifted the cellular program toward migration and adhesion (e.g., CXCR1, ITGA6), suggesting a specialized capacity for tumor homing and tissue infiltration rather than systemic cytokine release. Interestingly, the 4-1BB-CD3ζ construct displayed a prominent stress response and negative regulatory feedback loop (ATF3, HES1), reflecting the cell's internal attempt to mitigate the intense activation signal and prevent activation-induced cell death (AICD). The most profound genetic shifts were observed in advanced architecture. The third-generation construct CD28-41BB-ζ and

the dual-signaling hybrid construct CD28-ζ-γ demonstrated significant metabolic reprogramming. The marked upregulation of genes such as Nicotinamide N-methyltransferase (NNMT) and Sestrin 3 (SESN3) indicates an enhanced antioxidant defense mechanism and optimized energy flux. This metabolic fitness allows these cells to sustain long-term activity and maintain their functional integrity even when encountering low-density antigen environments in the solid tumor microenvironment. (Figure 5C-E).

To visualize the functional divergence driven by the different CAR architectures, we performed pathway enrichment analysis on the top 50 DEGs per construct. As depicted in the Enrichment Dot Plot, while the CD28-CD3ζ construct exhibited a highly significant enrichment in cytokine-cytokine receptor interactions (large, dark red nodes), the advanced architectures (third-generation construct CD28-41BB-ζ and the dual-signaling hybrid construct CD28-ζ-γ) uniquely engaged metabolic reprogramming and NAD+ pathways, highlighting their distinct functional fate under low-antigen conditions (Figure 5D).

Following the broad characterization of the transcriptomic landscape, where the top 50 most significant DEGs were mapped to distinct immunological pathways, it became imperative to dissect these functional shifts at a higher resolution. While pathway enrichment provides a macro-level understanding of the overarching cellular states (e.g., metabolic fitness vs. effector drive), it inherently masks the specific directionality—up-regulation versus down-regulation—of the critical individual genes that execute these states.

To bridge the gap between global pathway signatures and specific molecular mechanisms, we performed a targeted, gene-level directional analysis. Representative hallmark genes were isolated from the previously identified dominant pathways to evaluate their specific quantitative shifts ($|\log_2 \text{fold-change}| \geq 1.5$) following co-culture with low-antigen density targets. Crucially, by aligning these directional gene expression profiles with their respective CAR constructs, we aimed to directly attribute specific functional outputs to the underlying engineered intracellular elements. This approach allows us to deduce how individual signaling components—

such as the rapid glycolytic burst associated with CD28, the stress-modulation of 4-1BB, or the innate-like homing signals of FcRγ - mechanistically dictate the fate of the T cell at the single-gene level (Figure 5E). Comprehensive gene expression variations, including volcano plots mapping the magnitude of differential expression and exhaustive lists of significantly upregulated and downregulated genes for each specific CAR construct, are detailed in Supplementary Figure S3 and Supplementary Table S1.

Integrative Functional Scoring of TCRL-based CAR T-Cell Functionality Across Antigen Densities

To comprehensively evaluate the in vitro functional profiles of the distinct CAR architectures, we developed an exploratory multi-parametric functional framework that aggregates the readouts into a single efficacy score (Figure 6). For each CAR generation, individual assays were normalized using assay-level z-scores, followed by the subtraction of the matched Mock baseline to ensure that positive values reflect antigen-specific activity above background. Replicates were averaged for each CAR candidate and target, and the data were subsequently categorized into distinct biological modules: LDH cytotoxicity, cytokine secretion, activation marker expression, and inhibitory marker upregulation. The composite performance of each CAR candidate was formulated to mathematically balance aggressive tumor clearance with the risk of exhaustion. Weighting coefficients were assigned conceptually based on the hierarchical importance of primary effector functions in our acute assays: direct cytotoxicity was weighted highest (LDH contribution, 50%), followed by cytokine secretion (30%), and activation-support marker expression (20%), offset by an applied penalty for inhibitory marker induction (20%). The final integrated score (represented by the black dot in the plots) was calculated using the following weighted formula:

Final weighted score = 0.50 × LDH + 0.30 × cytokines + 0.20 × activation support −0.20 × inhibitory marker penalty − background penalty.

This integrative scoring system provides a quantitative functional hierarchy tool, which may predict how each CAR architecture negotiates the critical trade-offs between cytolytic potency and susceptibility to exhaustion across a gradient of antigen densities. The model highlights that the hybrid architecture achieves the highest global

efficacy scores at low antigen densities by minimizing the inhibitory marker penalty while sustaining robust cytotoxicity.

Discussion

1. Methodological Significance of the Normalized Biophysical Framework

The clinical implementation of Chimeric Antigen Receptor (CAR) T-cell therapy in solid tumors faces formidable obstacles that are fundamentally absent or less pronounced in hematological malignancies. These barriers include extreme target antigen heterogeneity, low-density antigen presentation, a highly hostile and immunosuppressive tumor microenvironment (TME), and the rapid onset of T-cell terminal exhaustion driven by chronic antigenic stimulation [25], [29]. Historical attempts to overcome these hurdles have frequently focused on escalating the binding affinity of the extracellular antigen-binding domain (scFv). However, excessive affinity often triggers a non-monotonic functional collapse, characterized by severe activation-induced cell death (AICD), off-tumor toxicities, and impaired tissue penetration due to an 'antigen sink' effect [10], [30]. To circumvent these confounding biophysical variables, this study established a highly sophisticated and rigorously controlled experimental system. By utilizing a TCR-like (TCRL) CAR targeting the melanoma-associated Tyr369-377/HLA-A2 complex, we locked the extracellular binding affinity at an empirically validated intermediate optimum (KD ~ 35nM) and utilized fluorescence-activated cell sorting (FACS) to carefully normalize surface receptor density (avidity) across all experimental cohorts [10]. This methodological normalization decoupled extracellular binding dynamics from intracellular signaling, allowing us to isolate and systematically interrogate how the structural architecture of the endodomain dictates T-cell fate, signal transduction, transcriptomic reprogramming, and functional longevity across a natural gradient of low, medium, and high target antigen densities.

2. Quantitative Signaling Thresholds: The Dichotomy Between CD3ζ and FcRγ

A foundational insight derived from our second-generation TCRL-based CAR T cells matrix is the absolute, non-interchangeable requirement for the CD3ζ cytoplasmic domain to execute primary antigen-specific cytolysis. Constructs relying exclusively on the FcRγ activation motif (CD28-FcRγ and 41BB-FcRγ) completely failed to elicit significant target cell death or robust lactate dehydrogenase (LDH) release, regardless of the antigen density presented by the target cells. From a structural standpoint, this functional deficit can be traced directly to the number and spatial orientation of Immunoreceptor Tyrosine-based Activation Motifs (ITAMs). The CD3ζ chain possesses three distinct ITAMs [12]. In contrast, the FcRγ chain harbors only a single ITAM, which predominantly recruits Syk or lower densities of ZAP-70 [31], [32]. Our functional data demonstrate that a single ITAM is quantitatively insufficient to cross the physical activation threshold required for lytic granule exocytosis in human primary T cells when extracellular avidity is kept constant. This is highly correlative with historical biophysical models of endogenous T-cell receptor (TCR) signaling, which indicate that a high density of accumulated phosphorylated ITAMs is necessary to stabilize the immunological synapse and form the macromolecular signaling clusters required for cytotoxic degranulation [33]. While FcRγ has been successfully used in some native immunoreceptors, its isolated deployment within a synthetic second-generation CAR configuration cannot compensate for the lack of multi-ITAM amplification provided by CD3ζ.

3. Costimulatory Kinetics and the Trade-off Between Efficacy and Exhaustion

Beyond primary activation, the temporal and quantitative kinetics of the intracellular response were strictly governed by the specific costimulatory domains integrated into the CAR endodomain. T cells equipped with the second-generation CD28-CD3ζ (28ζ) construct exhibited an immediate, high-magnitude burst of pro-inflammatory cytokines, specifically Interferon-gamma (IFN-γ) and Tumor Necrosis Factor-alpha (TNF-α), coupled with rapid up-regulation of the activation marker CD25. This hyper-acute activation pattern reflects the molecular wiring of the CD28 cytoplasmic tail, which possesses an YMNM motif that directly recruits phosphoinositide 3-kinase (PI3K) and activates the downstream Akt/mTOR axis [13]. While this rapid metabolic

and transcriptional induction yields potent short-term cytolytic effector functions, it is highly correlated with early, terminal differentiation and metabolic collapse under chronic antigen exposure [34], [35]. Recent studies in human melanoma demonstrate that such chronic TCR activation drives the accumulation of dysfunctional CD8+ T cells characterized by high co-inhibitory receptor expression (e.g., PD-1, TIM-3,LAG-3) and impaired mitochondrial bioenergetics [36]. This is directly supported by our supplementary phenotypic profiling, which demonstrates that 28ζ architectures inherently drive higher surface expression of co-inhibitory receptors such as CTLA-4 and LAG-3 compared to their BBζ counterparts following antigen encounter (Supplementary Figure S1). Conversely, the 41BB-CD3ζ (BBζ) construct displayed significantly more modulated initial kinetics, characterized by lower immediate cytokine release but enhanced functional persistence over multi-day target encounters. This fundamental difference in molecular routing preserves T-cell stemness and skews differentiation toward a central memory phenotype (T_CM). Crucially, phosphoproteomic and transcriptomic studies in the wider literature corroborate our observations, showing that 4-1BB signaling systematically dampens the over-activation of Lck, prevents tonic signaling-induced exhaustion, and promotes mitochondrial biogenesis and oxidative phosphorylation (OXPHOS), thereby rendering the cells highly resilient within an antigen-rich or chronic stimulation environment [32], [34]

4. Engineering Advanced Endo-domain Cooperativity Synergy to Overcome Low Antigen Densities

Antigen escape via transcriptional downregulation or clonal deletion represents one of the most pervasive escape mechanisms observed in solid tumor clinical trials [8]. When target cells present antigens below a specific density threshold, standard second-generation CARs typically fail to achieve the required signal summation, resulting in a state of operational ignorance. Our data reveals that this antigen-density barrier can be effectively dismantled by multiplexing costimulatory and activatory domains within a single CAR chain to lower the activation threshold without changing the extracellular affinity. The third-generation CD28-41BB-CD3ζ (28BBζ) construct and our novel hybrid architecture combining CD28-CD3ζ-FcRγ (28ζγ) demonstrated

unparalleled functional superiority against low and medium antigen-density targets. Interestingly, this synergy was found to be highly position-dependent. The 28ζγ orientation (where CD3ζ is membrane-proximal and FcRγ is C-terminal) mediated significantly higher specific lysis and cytokine expression compared to the flipped 28γζ configuration. This structural variance suggests that spatial and steric constraints within the synthetic endodomain heavily influence the recruitment and structural stability of downstream adapter proteins. The distal positioning of FcRγ likely minimizes steric hindrance around the multi-ITAM CD3ζ core, allowing for the concurrent docking of ZAP-70 and alternative tyrosine kinases like Syk [37]. Our supplementary functional comparisons robustly validate this spatial hypothesis; altering the sequence to a membrane-proximal FcRγ (CD28-FcRγ-CD3ζ) significantly blunts the cytolytic response. Moreover, attempting to bypass CD3ζ entirely by utilizing FcRγ alongside dual costimulation (CD28-41BB-FcRγ) results in complete functional failure (Supplementary Figure S2), proving that enhanced costimulation cannot compensate for an inadequate primary ITAM foundation. By optimizing this spatial configuration, we achieved an artificial signal-transduction that amplifies weak antigenic inputs into a robust transcriptional and cytolytic program, directly overcoming the operational limitations of conventional CAR setups against heterogeneous solid tumors.

5. Transcriptomic and Metabolic Reprogramming: Uncoupling Activation from Exhaustion

To uncover the deeper gene regulatory networks driving these distinct phenotypic behaviors, we performed global transcriptomic profiling via bulk RNA-sequencing following exposure to low-antigen targets. The transcriptomic landscape confirmed that the physical composition of the endodomain fundamentally rewires the global genetic architecture of the cell. The sheer magnitude and directionality of these unique transcriptomic shifts—from the chemokine-heavy profile of 28ζ to the metabolic endurance signature of the hybrid architectures—are comprehensively captured in the volcano plots and differential expression datasets provided in Supplementary Figure S3 and Supplementary Table S1, serving as a foundational reference for the rational design of targeted cellular states. An unexpected and highly

notable finding was observed in the CD28-FcRγ (28γ) cohort: despite its complete cytolytic incompetence due to the absence of CD3ζ, this construct exhibited a specialized transcriptomic signature heavily enriched for cell migration, chemotaxis, and cellular adhesion, characterized by the robust up-regulation of CXCR1 and Integrin Subunit Alpha 6 (ITGA6) [38]. This finding indicates that while a single ITAM cannot drive degranulation, it can selectively activate the chemokine receptor and integrin pathways, providing a potential modular framework for engineering specialized tumor-homing vehicles. More profoundly, our top-performing functional architectures (28BBζ and 28ζγ) demonstrated a remarkable capacity to decouple potent primary activation from the downstream trajectory of terminal exhaustion. When exposed to limiting antigen densities, these constructs did not exhibit the classic transcriptional signatures of T-cell exhaustion—typically defined by the synchronized upregulation of co-inhibitory receptors (PD-1, CTLA-4, LAG-3, and TIM-3) and the exhaustion-associated transcription factor TOX [39]. Instead, they engaged an advanced metabolic and survival program, characterized by the marked upregulation of Nicotinamide N-methyltransferase (NNMT) and Sestrin 3 (SESN3). NNMT acts as a metabolic gatekeeper, regulating intracellular nicotinamide adenine dinucleotide (NAD+) salvage pathways and modulating histone methylation patterns to lock the chromatin in a state of high functional plasticity [40]. The critical importance of preserving intracellular NAD+ pools has been recently underscored in human melanoma explant models, where CD38-mediated NAD+ depletion driven by chronic T cell stimulation was shown to induce metabolic dysfunction, reduce TCF7 expression, and enforce terminal exhaustion [36]. By intrinsically upregulating NAD+ salvage mechanisms via NNMT, our advanced hybrid architectures likely counteract similar metabolic depletion, providing a mechanistic basis for their superior longevity. Concurrently, Sestrin 3 (SESN3) functions as an intracellular sensor that suppresses reactive oxygen species (ROS) accumulation and fine-tunes the AMPK/mTOR metabolic axis to protect cells from oxidative stress-induced apoptosis under prolonged activation [41]. This combined metabolic and transcriptomic rewiring ensures that 28BBζ and 28ζγ CAR T-cells maintain high mitochondrial and energetic fitness, enabling them to execute potent acute multi-target cytotoxic capacity in vitro. While these short-term assays do not show the early transcriptional signatures of

exhaustion, future in vivo studies and prolonged serial killing models are required to validate their durable resistance to terminal exhaustion over time.

6. Integrative Functional Scoring

The translation of CAR T-cell therapy to solid tumors necessitates an intricate balance between robust activation against heterogeneous, low-density antigens and the prevention of premature functional exhaustion. To address this multidimensional challenge, we developed a weighted multi-parametric scoring system (Figure 6) that serves as an integrative functional framework for CAR T-cell fitness in vitro. We assigned conceptual weights based on primary functional priorities: 50% for direct cytolysis (LDH release), 30% for effector cytokine production, and 20% for activation marker support, offset by a 20% penalty for inhibitory marker induction. This integrative framework provides a holistic visualization highlighting the functional trajectory of various CAR architectures in an acute setting, establishing a foundation for future predictive models. Importantly, it corroborates our empirical findings regarding the superiority of the novel hybrid constructs, demonstrating that a balanced signaling architecture can maximize the 'efficacy score' by uncoupling cytolytic output from exhaustive penalties. Beyond the scope of this study, this integrative multi-parametric methodology establishes a quantitative foundation for the rational design of future immunotherapies. It allows researchers to computationally anticipate the efficacy and safety profiles of newly engineered T-cells prior to clinical translation, representing a significant conceptual advancement in the field of synthetic immunology[9].

7. Analytical Power and Future Therapeutic Blueprint of the Research System

In conclusion, our comprehensive functional, biophysical, and transcriptomic characterization establishes a clear paradigm for the future design of adoptive cell immunotherapies. We demonstrate that the intracellular signaling endo-domain can be rationally calibrated to override external biophysical limitations, ensuring robust effector function against low-density solid tumor antigens while completely averting early exhaustion. Crucially, the foundational potential of this work resides in the

intrinsic power of the experimental system we have created. By normalizing all external biophysical variables—specifically keeping affinity fixed at an optimal baseline and standardizing surface avidity—we have engineered a clean, high-resolution analytical platform that can be deployed to systematically map and decode the functional output of any novel synthetic intracellular domain, signaling motif, or combination thereof. Rather than relying on trial-and-error configurations that are frequently confounded by unpredictable extracellular binding kinetics, this platform provides a highly predictable, standardized benchmark for the rational engineering of synthetic immunoreceptors. Ultimately, this system serves as a powerful discovery and validation engine, offering an optimized, transferable blueprint to accelerate the development of highly resilient, metabolically superior cell-based therapies capable of eradicating antigen-poor solid malignancies.

References

[1] Y. Wang, F. Luo, J. Yang, C. Zhaov, and Y. Chu, "New chimeric antigen receptor design for solid tumors," Dec. 22, 2017, *Frontiers Media S.A.* doi: 10.3389/fimmu.2017.01934.

[2] C. H. June, R. S. O'Connor, O. U. Kawalekar, S. Ghassemi, and M. C. Milone, "CAR T cell immunotherapy for human cancer," *Science (1979).*, vol. 359, no. 6382, pp. 1361–1365, 2018, doi: 10.1126/science.aar6711.

[3] M. Martinez and E. K. Moon, "CAR T cells for solid tumors: New strategies for finding, infiltrating, and surviving in the tumor microenvironment," *Front. Immunol.*, vol. 10, no. FEB, pp. 1–21, 2019, doi: 10.3389/fimmu.2019.00128.

[4] R. Oren *et al.*, “Functional Comparison of Engineered T Cells Carrying a Native TCR versus TCR-like Antibody–Based Chimeric Antigen Receptors Indicates Affinity/Avidity Thresholds,” *The Journal of Immunology*, vol. 193, no. 11, 2014, doi: 10.4049/jimmunol.1301769.

[5] M. Poorebrahim, N. Mohammadkhani, R. Mahmoudi, M. Gholizadeh, E. Fakhr, and A. Cid-Arregui, “TCR-like CARs and TCR-CARs targeting neoepitopes: an emerging potential,” *Cancer Gene Ther.*, vol. 28, no. 6, pp. 581–589, 2021, doi: 10.1038/s41417-021-00307-7.

[6] S. Mehrotra *et al.*, “A Coreceptor-Independent Transgenic Human TCR Mediates Anti-Tumor and Anti-Self Immunity in Mice,” *The Journal of Immunology*, vol. 189, no. 4, pp. 1627–1638, 2012, doi: 10.4049/jimmunol.1103271.

[7] A. J. Walker *et al.*, “Tumor Antigen and Receptor Densities Regulate Efficacy of a Chimeric Antigen Receptor Targeting Anaplastic Lymphoma Kinase,” *Molecular Therapy*, vol. 25, no. 9, pp. 2189–2201, 2017, doi: 10.1016/j.ymthe.2017.06.008.

[8] R. G. Majzner *et al.*, “Tuning the antigen density requirement for car T-cell activity,” *Cancer Discov.*, vol. 10, no. 5, pp. 702–723, 2020, doi: 10.1158/2159-8290.CD-19-0945.

[9] R. Greenman *et al.*, “Phenotypic models of CAR T-Cell activation elucidate the pivotal regulatory role of CAR downmodulation,” *Mol. Cancer Ther.*, vol. 20, no. 5, pp. 946–957, May 2021, doi: 10.1158/1535-7163.MCT-19-1110.

[10] R. Greenman *et al.*, “Shaping functional avidity of CAR T Cells: Affinity, avidity, and antigen density that regulate response,” *Mol. Cancer Ther.*, vol. 20, no. 5, pp. 872–884, May 2021, doi: 10.1158/1535-7163.MCT-19-1109.

[11] A. H. Long *et al.*, “4-1BB costimulation ameliorates T cell exhaustion induced by tonic signaling of chimeric antigen receptors,” *Nat. Med.*, vol. 21, no. 6, pp. 581–590, 2015, doi: 10.1038/nm.3838.

[12] A. I. Salter *et al.*, “Phosphoproteomic analysis of chimeric antigen receptor signaling reveals kinetic and quantitative differences that affect cell function,” *Sci. Signal.*, vol. 11, no. 544, pp. 1–18, 2018, doi: 10.1126/scisignal.aat6753.

[13] O. U. Kawalekar *et al.*, “Distinct Signaling of Coreceptors Regulates Specific Metabolism Pathways and Impacts Memory Development in CAR T Cells,” *Immunity*, vol. 44, no. 3, p. 712, Mar. 2016, doi: 10.1016/j.immuni.2016.02.023.

[14] M. C. Ramello *et al.*, “HHS Public Access,” vol. 12, no. 568, 2019, doi: 10.1126/scisignal.aap9777.An.

[15] K. Oved *et al.*, “A Novel Postpriming Regulatory Check Point of Effector/Memory T Cells Dictated through Antigen Density Threshold-Dependent Anergy,” *The Journal of Immunology*, vol. 178, no. 4, pp. 2307–2317, Feb. 2007, doi: 10.4049/jimmunol.178.4.2307.

[16] D. Tovar Manzano *et al.*, “Tumor-infiltrating lymphocyte expansion protocols for adoptive cell therapy in cancer,” Dec. 01, 2025, *Springer Science and Business Media B.V.* doi: 10.1007/s13402-025-01112-2.

[17] S. Picelli, Å. K. Björklund, O. R. Faridani, S. Sagasser, G. Winberg, and R. Sandberg, “Smart-seq2 for sensitive full-length transcriptome profiling in single cells,” *Nat. Methods*, vol. 10, no. 11, pp. 1096–1100, Nov. 2013, doi: 10.1038/nmeth.2639.

[18] S. Picelli, Å. K. Björklund, B. Reinius, S. Sagasser, G. Winberg, and R. Sandberg, “Tn5 transposase and tagmentation procedures for massively scaled sequencing projects,” *Genome Res.*, vol. 24, no. 12, pp. 2033–2040, Dec. 2014, doi: 10.1101/gr.177881.114.

[19] A. Dobin *et al.*, “STAR: Ultrafast universal RNA-seq aligner,” *Bioinformatics*, vol. 29, no. 1, pp. 15–21, Jan. 2013, doi: 10.1093/bioinformatics/bts635.

[20] G. H. Putri, S. Anders, P. T. Pyl, J. E. Pimanda, and F. Zanini, “Analysing high-throughput sequencing data in Python with HTSeq 2.0,” *Bioinformatics*, vol. 38, no. 10, pp. 2943–2945, May 2022, doi: 10.1093/bioinformatics/btac166.

[21] M. I. Love, W. Huber, and S. Anders, “Moderated estimation of fold change and dispersion for RNA-seq data with DESeq2,” *Genome Biol.*, vol. 15, no. 12, Dec. 2014, doi: 10.1186/s13059-014-0550-8.

[22] J. Köster and S. Rahmann, “Snakemake-a scalable bioinformatics workflow engine,” *Bioinformatics*, vol. 28, no. 19, pp. 2520–2522, 2012, doi: 10.1093/bioinformatics/bts480.

[23] J. Huang *et al.*, “The kinetics of two-dimensional TCR and pMHC interactions determine T-cell responsiveness,” *Nature*, vol. 464, no. 7290, 2010, doi: 10.1038/nature08944.

[24] D. H. Lynch, “The promise of 4-1BB (CD137)-mediated immunomodulation and the immunotherapy of cancer,” *Immunol Rev*, vol. 222, pp. 277–286, 2008.

[25] T. F. Gajewski, H. Schreiber, and Y.-X. Fu, “Innate and adaptive immune cells in the tumor microenvironment,” *Nat. Immunol.*, vol. 14, no. 10, pp. 1014–1022, 2013, doi: 10.1038/ni.2703.

[26] K. Watanabe *et al.*, “Target Antigen Density Governs the Efficacy of Anti–CD20-CD28-CD3 ζ Chimeric Antigen Receptor–Modified Effector CD8+ T Cells,” *The Journal of Immunology*, vol. 194, no. 3, pp. 911–920, Feb. 2015, doi: 10.4049/jimmunol.1402346.

[27] J. G. Crompton, M. Sukumar, and N. P. Restifo, “Uncoupling T-cell expansion from effector differentiation in cell-based immunotherapy,” *Immunol. Rev.*, vol. 257, no. 1, pp. 264–276, 2014, doi: 10.1111/imr.12135.

[28] J. Feucht *et al.*, “Calibration of CAR activation potential directs alternative T cell fates and therapeutic potency,” *Nat. Med.*, vol. 25, no. 1, pp. 82–88, Jan. 2019, doi: 10.1038/s41591-018-0290-5.

[29] E. J. Wherry and M. Kurachi, “Molecular and cellular insights into T cell exhaustion,” *Nat. Rev. Immunol.*, vol. 15, no. 8, pp. 486–499, 2015, doi: 10.1038/nri3862.

[30] M. Chmielewski, A. Hombach, C. Heuser, G. P. Adams, and H. Abken, “T Cell Activation by Antibody-Like Immunoreceptors: Increase in Affinity of the Single-Chain Fragment Domain above Threshold Does Not Increase T Cell Activation against Antigen-Positive Target Cells but Decreases Selectivity,” *The Journal of Immunology*, vol. 173, no. 12, 2004, doi: 10.4049/jimmunol.173.12.7647.

[31] H. Abken, “Driving CARs on the Highway to Solid Cancer: Some Considerations on the Adoptive Therapy with CAR T Cells,” *Hum. Gene Ther.*, vol. 28, no. 11, pp. 1047–1060, 2017, doi: 10.1089/hum.2017.115.

[32] J. Feucht *et al.*, “Calibration of CAR activation potential directs alternative T cell fates and therapeutic potency,” 2019. doi: 10.1038/s41591-018-0290-5.

[33] O. Dushek and P. A. Van der Merwe, “An induced rebinding model of antigen discrimination,” *Trends Immunol.*, vol. 35, no. 4, pp. 153–158, 2014, doi: 10.1016/j.it.2014.02.002.

[34] K. G. Daniels *et al.*, “Decoding CAR T cell phenotype using combinatorial signaling motif libraries and machine learning,” *Science (1979).*, vol. 378, no. 6625, pp. 1194–1200, 2022, doi: 10.1126/science.abq0225.

[35] L. Labanieh, R. G. Majzner, and C. L. Mackall, “Programming CAR-T cells to kill cancer,” *Nat. Biomed. Eng.*, vol. 2, no. 6, pp. 377–391, 2018, doi: 10.1038/s41551-018-0235-9.

[36] O. Y. Revach *et al.*, “Overcoming resistance to immunotherapy by targeting CD38 in human tumor explants,” *Cell Rep. Med.*, vol. 6, no. 7, p. 102210, 2025, doi: 10.1016/j.xcrm.2025.102210.

[37] S. Ghorashian *et al.*, “Enhanced CAR T cell expansion and prolonged persistence in pediatric patients with ALL treated with a low-affinity CD19 CAR,” *Nat. Med.*, vol. 25, no. 9, pp. 1408–1414, 2019, doi: 10.1038/s41591-019-0549-5.

[38] C. Y. Slaney, M. H. Kershaw, and P. K. Darcy, “Trafficking of T cells into tumors,” *Cancer Res.*, vol. 74, no. 24, pp. 7168–7174, 2014, doi: 10.1158/0008-5472.CAN-14-2458.

[39] O. Khan *et al.*, “TOX transcriptionally and epigenetically programs CD8+ T cell exhaustion,” *Nature*, vol. 571, no. 7764, pp. 211–218, 2019, doi: 10.1038/s41586-019-1325-x.

[40] M. Peng *et al.*, “Aerobic glycolysis promotes T helper 1 cell differentiation through an epigenetic mechanism,” *Science (1979).*, vol. 6284, no. September, pp. 481–485, 2016, doi: 10.1126/science.aaf6284.Aerobic.

[41] L. Chantranupong *et al.*, “The sestrins interact with gator2 to negatively regulate the amino-acid-sensing pathway upstream of mTORC1,” *Cell Rep.*, vol. 9, no. 1, pp. 1–8, 2014, doi: 10.1016/j.celrep.2014.09.014.

Figure Legends

Figure 1: Design of a stringently controlled biophysical system for CAR evaluation.

(A) Schematic representation of the experimental model controlling for Affinity (fixed at ~35nM), Avidity (normalized via GFP sorting), and Antigen Density (graduated

across natural cell lines). (B) The basic CAR scaffold - the schematic diagram of the CAR design. (C) Diagram of the modular CAR constructs incorporating 8 varying combinations of CD28, 4-1BB, CD3ζ, and FcRγ. (D) Representative flow-cytometry Dot Plots showing GFP vs. Surface CAR expression staining in sorted T cells. (E) Representative flow-cytometry histograms illustrating quantification establishing a gradient of A2-Tyr antigen density with 1938, 526, Skmel23, 501.A natural melanoma cell lines. Results shown in (D) represent 3 independent experiments, all performed separately for T cells of each of the N=3 independent biological donors.

Figure 2: Cytolytic and functional profiling of 2nd generation TCRL-CARs.

(A) Cytotoxicity of untransduced (Mock), 2nd generation TCRL-CARs T cells against melanoma targets at a fixed effector-to-target ratio (E:T = 10:1) (N=2 independent biological donors, n = 6 total technical replicates). (B-C) Expression of activation markers following stimulation with low/medium/high density antigen targets. CD25 and 4-1BB expression (MFI) were measured at 24 h. Data are shown as mean ± SEM (n = 3 biological replicates). (D) Heatmap summarizing adjusted p-values for combined all normalized cytokine secretion assays (IFNγ and TNF-α) of the CAR T cells measured by ELISA following co-culture with melanoma cell lines at an effector-to-target ratio (E:T) of 1:1 for 18 h. (N=2 independent biological donors, n = 3 total technical replicates). (E) Representative violin-plot of the IFN-γ amount secreted individually in an experiment measured by picograms per milliliter. (F) Summarized functional outputs evaluating cytotoxicity, cytokine secretion and activation markers for 2nd-generation TCRL-CARs T cells against melanoma targets, we combined all normalized datasets and analyzed each CAR–target pair. Outliers were removed using a median absolute deviation (MAD)– based filter. Group normality was assessed with the Shapiro–Wilk test, and statistical comparisons were chosen accordingly: normally distributed groups were evaluated using Welch's t-test (which does not assume equal variances), whereas non-normal groups were evaluated using the Mann–Whitney U test. Multiple comparisons were corrected with the Benjamini–Hochberg FDR method, and only combinations whose mean normalized activation exceeded the

mock baseline were considered biologically meaningful. The resulting adjusted p-values were summarized in a heatmap, highlighting which TCRL-based CAR types demonstrated significantly elevated activity toward each target.

For (A), (B) and (C), statistical significance was determined by two-way ANOVA (*P < 0.05; **P < 0.01; ***P < 0.001; ****P < 0.0001).

Figure 3: Enhanced functional sensitivity of 3rd-generation and hybrid architectures.

(A) Cytotoxicity of untransduced (Mock), 3rd generation TCRL-CARs T cells against melanoma targets after 4 h co-culture at a fixed effector-to-target ratio (E:T = 10:1) (N=2 independent biological donors, n = 5 total technical replicates). Data are shown as mean ± SEM. (B) Same data presented in Heatmap summarizing adjusted p-values for normalized cytotoxicity assay of the CAR T cells. (C) Heatmap summarizing adjusted p-values for combined all normalized cytokine secretion assays (IFNγ and TNF-α) together with cytotoxicity assay of the CAR T cell; cytokines were measured by ELISA following co-culture with melanoma cell lines at an effector-to-target ratio (E:T) of 1:1 for 18 h. (N=2 independent biological donors, n = 2 total technical replicates). (D) Representative violin-plot of the TNF-α amount secreted individually in an experiment measured by picograms per milliliter. (E) Functional screen of the experimental population distribution. Strip plot of normalized results of different assays, each point corresponds to a single measurement, the color denotes the CAR construct, and the marker shape identifies the assay.

For (A) statistical significance was determined by two-way ANOVA (*P < 0.05; **P < 0.01; ***P < 0.001; ****P < 0.0001).

Figure 4: Multiparametric identification of optimal CAR architectures.

(A) Representative Effector-to-target ratio–dependent killing of natural melanoma cell lines with gradient of A2-Tyr antigen density by 2nd and 3rd generation TCRL-based CAR T cells. (B) Functional screen of the experimental population distribution. Strip-plot of

Z-score normalized activation metrics visualizing the distribution of cellular responses. (C) Heatmap summarizing adjusted p-values for combined all normalized cytokine secretion assays (IFNγ and TNF-α) of the CAR T cells measured by ELISA following co-culture with melanoma cell lines at an effector-to-target ratio (E:T) of 1:1 for 18 h. (N=2, n = 3 independent experiments). (D) Heatmap showing sustained expression of combined activation markers (CD25+4-1BB) of the CAR T cells measured by flow-cytometry (MFI) following co-culture with melanoma cell lines at an effector-to-target ratio (E:T) of 1:1 for 18 h. (N=2 independent biological donors, n = 3 total technical replicates). (E) Heatmap summarizing adjusted p-values for normalized cytotoxicity assay of the 2nd and 3rd generation TCRL-based CARs T cells against melanoma targets after 4 h co-culture at a fixed effector-to-target ratio (E:T = 10:1) (N=2, n = 5 biological replicates). (F) Normalized expression graphs of combined inhibitory markers (PD-1+CTLA-4+LAG-3+TIM-3) measured by flow-cytometry (MFI) following co-culture with melanoma cell lines at an effector-to-target ratio (E:T) of 1:1 for 18 h. (N=2 independent biological donors, n = 3 total technical replicates).

Figure 5: Transcriptomic signatures and metabolic reprogramming driven by CAR architecture.

(A) PCA plot of isolated (solo) cell samples. The analysis demonstrates distinct global gene expression clustering among the different cell populations. PC1, accounting for 84% of the variance, primarily drives the separation between the effector cells (All CARs, T-only samples) and the target melanoma cell lines (Melanoma 1938, negative control; Melanoma 526, low antigen density). (B) PCA plot encompassing all experimental conditions, including solo cultures and CAR-T/melanoma co-cultures. The inclusion of co-cultured samples reveals distinct transcriptomic shifts. Arrows indicate sub-clusters of samples characterized as "more transcriptionally active" versus "less transcriptionally active," reflecting the varying degrees of CAR-T cell activation and cellular response upon interaction with the different tumor models. Data represents bulk RNA-seq derived from N=4 biological replicates per condition. (C) Bar graph representing the relative enrichment and functional dominance of the primary immunological pathways identified for each CAR construct. Pathway

signatures were derived from differential expression analysis (RNA-seq) comparing CAR-T cells cultured alone versus CAR-T cells co-cultured with 526 melanoma target cells (characterized by low-density target antigen expression). For each construct, the analysis focused on the top 50 most variable genes, which were classified as significantly up-regulated or down-regulated utilizing strict statistical thresholds of $|\log_2 \text{fold-change}| \geq 1.5$ and an adjusted p-value ≤ 0.05. (D) The dot plot illustrates the functional pathway enrichment across the distinct TCRL-CAR constructs. Node size (Gene Count) represents the absolute number of differentially expressed genes (out of the top 50 analyzed) that map to a specific immunological pathway. Node color (Significance Level) indicates the statistical robustness of the pathway enrichment, expressed as log10 {adjusted P -value}; darker red hues denote higher statistical significance. (E) Horizontal bar chart depicting the log2 fold-change of representative differentially expressed genes (DEGs) across distinct immunological pathways. The analysis compares TCRL-CAR T cells co-cultured with target cells (526 melanoma) versus T cells alone. The vertical dashed red lines demarcate the established significance thresholds. Positive values indicate significant up-regulation, while negative values represent down-regulated genes.

Figure 6: An Integrative Functional Scoring Framework for CAR T-Cell Efficacy and Exhaustion

Integrative evaluation of CAR candidates across variable antigen densities. For each CAR generation, raw values from every assay were normalized independently using assay-level z-scores. The matched Mock baseline was subtracted to isolate CAR-specific activity above background. Biological replicates were averaged for each CAR candidate and target, and subsequently grouped into four biological functional modules: LDH cytotoxicity, cytokines, activation markers, and inhibitory markers. The composite performance of each CAR is represented by the Final weighted score (black dots), calculated as follows: Final weighted score = 0.50 × LDH + 0.30 × cytokines + 0.20× activation support − 0.20 × inhibitory marker penalty − background penalty. This visualization serves as a predictive tool, illustrating the exact balance between target eradication capacity and functional exhaustion for each tested architecture.

Supplementary Figure Legends

Supplementary Figure S1. Profiling Inhibitory Markers and Cytolytic Efficacy in 2ND Generation Architectures

(A) Normalized Cytotoxicity Heatmap: Summarized adjusted p-values LDH release data for 2nd generation constructs across a gradient of antigen densities (N=2 independent biological donors, n = 6 total technical replicates).(B) Comparative Cytolysis: Bar graphs showing percentage cytotoxicity for lead 2nd generation TCRL-CARs T cells candidates (e.g., CD28-CD3ζ vs. 4-1BB-CD3ζ) against melanoma targets after 4 h co-culture at a fixed effector-to-target ratio (E:T = 10:1) (N=2 independent biological donors, n = 4 total technical replicates). Data are shown as mean ± SEM. (C) Heatmap of Combined Inhibitory Marker Expression: Normalized adjusted p-values expression of PD-1, CTLA-4, LAG-3, and TIM-3 following 20-hour co-culture with melanoma targets. (N=2 independent biological donors, n = 5 total technical replicates). (D-E) Individual Marker Analysis: MFI quantification of CTLA-4 and LAG-3 across low, medium, and high antigen densities, showing no significant differences between CD28 and 4-1BB signaling in the absence of chronic stimulation. (N=2 independent biological donors, n = 5 total technical replicates). Data are shown as mean ± SEM. For (B), (D) and (E), statistical significance was determined by two-way ANOVA (*P < 0.05; **P < 0.01; ***P < 0.001; ****P < 0.0001).

Supplementary Figure S2: Functional Synergy and Position-Dependent Signaling in 3RD Generation and Hybrid CARs

(A) 3rd Generation Costimulatory Synergy: Comparative Cytotoxicity of 28BBζ vs. variants lacking CD3ζ, demonstrating the absolute requirement for the zeta chain for primary cytolysis even in complex architectures. (N=1 independent biological donor, n = 4 total technical replicates). (B) Position-Dependent Synergy in Hybrid Constructs: Comparison of specific lysis between 28ζγ (C-terminal FcRγ) and 28γζ (flipped orientation), highlighting the superior signal amplification of the 28ζγ configuration. (N=1 independent biological donor, n = 4 total technical replicates). (C) Competitive

Functional Sensitivity: Competitive comparison between 2nd generation (28ζ) and hybrid (28ζγ) constructs against low-antigen density targets.

Bar graphs showing percentage cytotoxicity for TCRL-CARs T cells candidates against melanoma targets after 4 h co-culture at a fixed effector-to-target ratio (E:T = 10:1). Data are shown as mean ± SEM. For (A), (B) and (C), statistical significance was determined by two-way ANOVA (*P < 0.05; **P < 0.01; ***P < 0.001; ****P < 0.0001).

Supplementary Figure S3: Construct-Specific Transcriptomic Fingerprints Following Antigen Encounter

(A-F) Volcano Plots of Differential Gene Expression profilies: Global transcriptional changes in six distinct CAR architectures—(A) 28ζ, (B) 28γ, (C) BBζ, (D) BBγ, (E) 28BBζ, and (F) 28ζγ—following encounter with low-antigen targets (Melanoma 526) compared to isolated baseline. The x-axis represents the Log2 fold change in gene expression, and the y-axis indicates statistical significance as log {10} adjusted p-value. Genes significantly upregulated upon target cell encounter are highlighted in red, while significantly downregulated genes are shown in blue. Grey points indicate genes that did not meet the significance thresholds. Data represents bulk RNA-seq derived from N=4 independent biological donors per condition.

Supplementary Table S1: Comprehensive List of Differentially Expressed Genes (DEGs)

Top 50 Upregulated and Downregulated Genes per CAR Architecture Description: This table details the gene names and directional shifts used to identify the functional specialization of each construct.

Figure 1

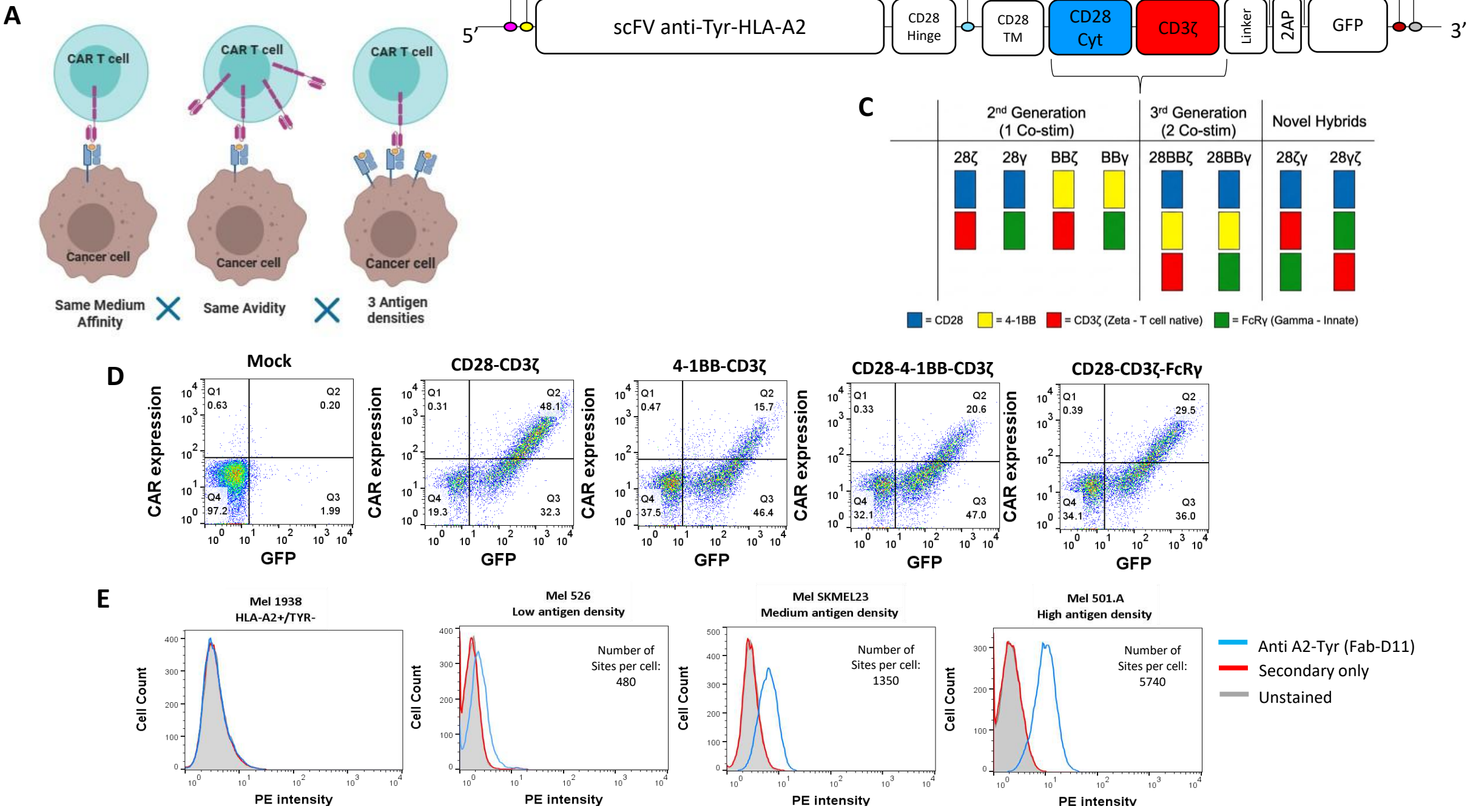

A
CAR T cell
Cancer cell
Same Medium Affinity
Same Avidity
3 Antigen densities
B
EcoRI
NcoI
SacII
HpaI
SphI
BglII
BamHI
5'
scFV anti-Tyr-HLA-A2
CD28 Hinge
CD28 TM
CD28 Cyt
CD3ζ
Linker
2AP
GFP
3'
C
2nd Generation (1 Co-stim)
3rd Generation (2 Co-stim)
Novel Hybrids
28ζ
28γ
BBζ
BBγ
28BBζ
28BBγ
28ζγ
28γζ
= CD28
= 4-1BB
= CD3ζ (Zeta - T cell native)
= FcRγ (Gamma - Innate)
D
Mock
CD28-CD3ζ
4-1BB-CD3ζ
CD28-4-1BB-CD3ζ
CD28-CD3ζ-FcRγ
CAR expression
GFP
Q1 0.63
Q2 0.20
Q4 97.2
Q3 1.99
Q1 0.31
Q2 48.1
Q4 19.3
Q3 32.3
Q1 0.47
Q2 15.7
Q4 37.5
Q3 46.4
Q1 0.33
Q2 20.6
Q4 32.1
Q3 47.0
Q1 0.39
Q2 29.5
Q4 34.1
Q3 36.0
E
Mel 1938
HLA-A2+/TYR-
Mel 526
Low antigen density
Number of Sites per cell: 480
Mel SKMEL23
Medium antigen density
Number of Sites per cell: 1350
Mel 501.A
High antigen density
Number of Sites per cell: 5740
Cell Count
PE intensity
Anti A2-Tyr (Fab-D11)
Secondary only
Unstained

Figure 2

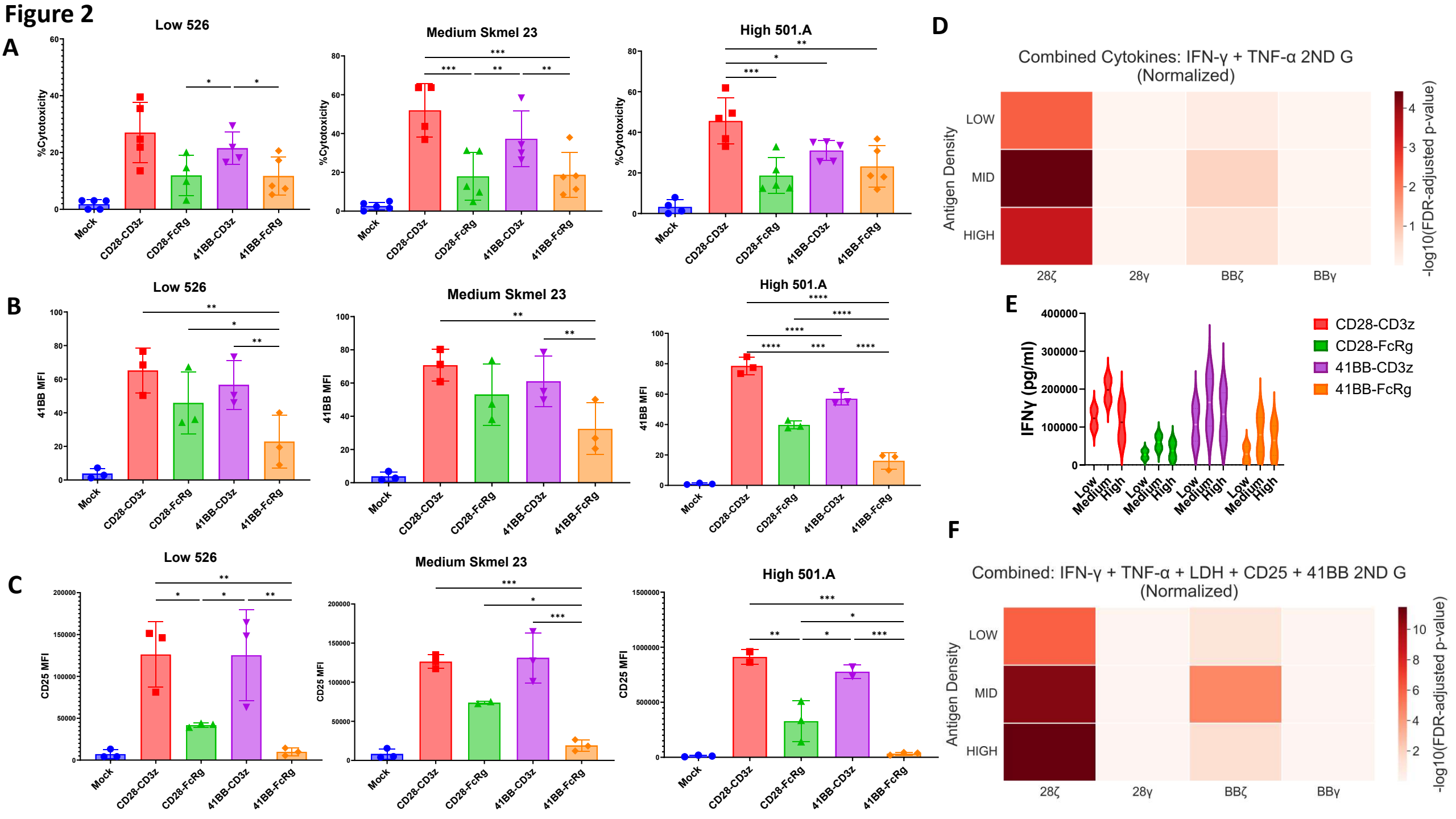
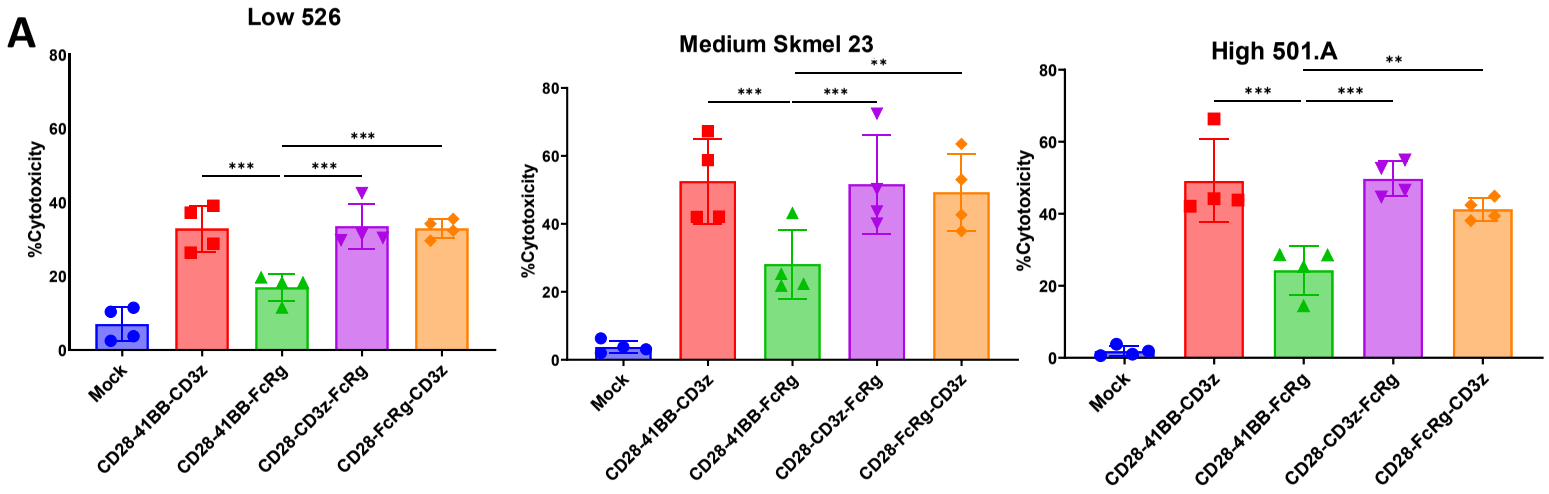
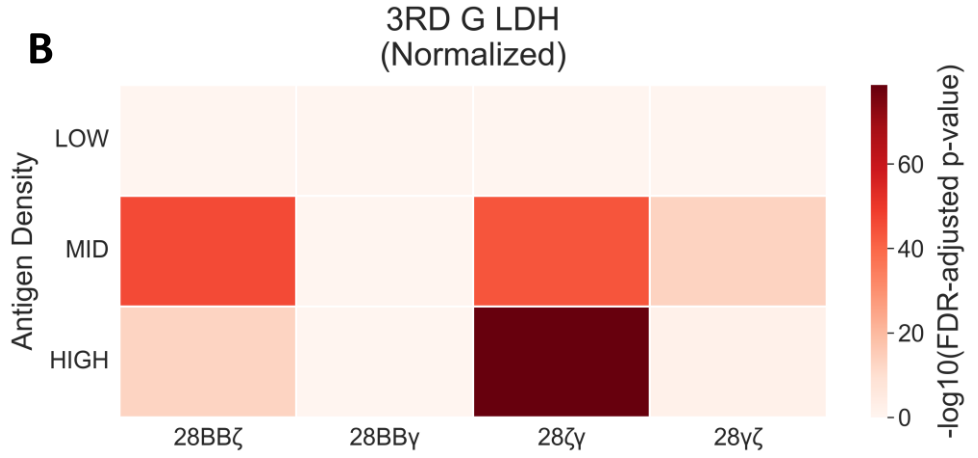
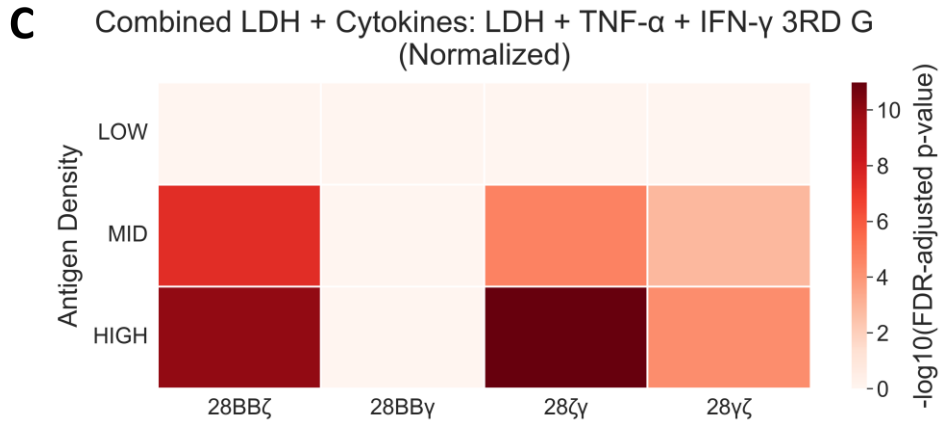
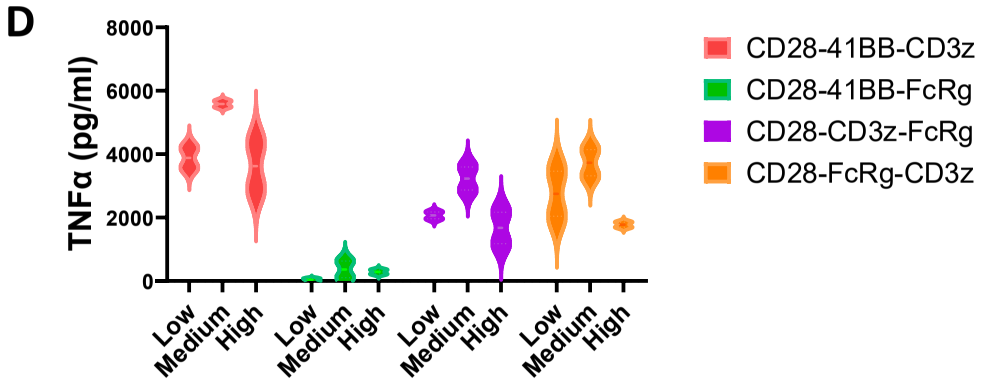

A
Low 526
Medium Skmel 23
High 501.A
%Cytotoxicity
B
41BB MFI
C
CD25 MFI
Mock
CD28-CD3z
CD28-FcRg
41BB-CD3z
41BB-FcRg
D
Combined Cytokines: IFN-γ + TNF-α 2ND G (Normalized)
Antigen Density
LOW
MID
HIGH
28ζ
28γ
BBζ
BBγ
-log10(FDR-adjusted p-value)
E
IFNγ (pg/ml)
Low
Medium
High
F
Combined: IFN-γ + TNF-α + LDH + CD25 + 41BB 2ND G (Normalized)

Figure 3


A
Low 526
Medium Skmel 23
High 501.A
%Cytotoxicity
Mock
CD28-41BB-CD3z
CD28-41BB-FcRg
CD28-CD3z-FcRg
CD28-FcRg-CD3z


B
3RD G LDH
(Normalized)
Antigen Density
LOW
MID
HIGH
28BBζ
28BBγ
28ζγ
28γζ
-log10(FDR-adjusted p-value)


C
Combined LDH + Cytokines: LDH + TNF-α + IFN-γ 3RD G
(Normalized)
Antigen Density
LOW
MID
HIGH
28BBζ
28BBγ
28ζγ
28γζ
-log10(FDR-adjusted p-value)


D
TNFα (pg/ml)
Low
Medium
High
CD28-41BB-CD3z
CD28-41BB-FcRg
CD28-CD3z-FcRg
CD28-FcRg-CD3z

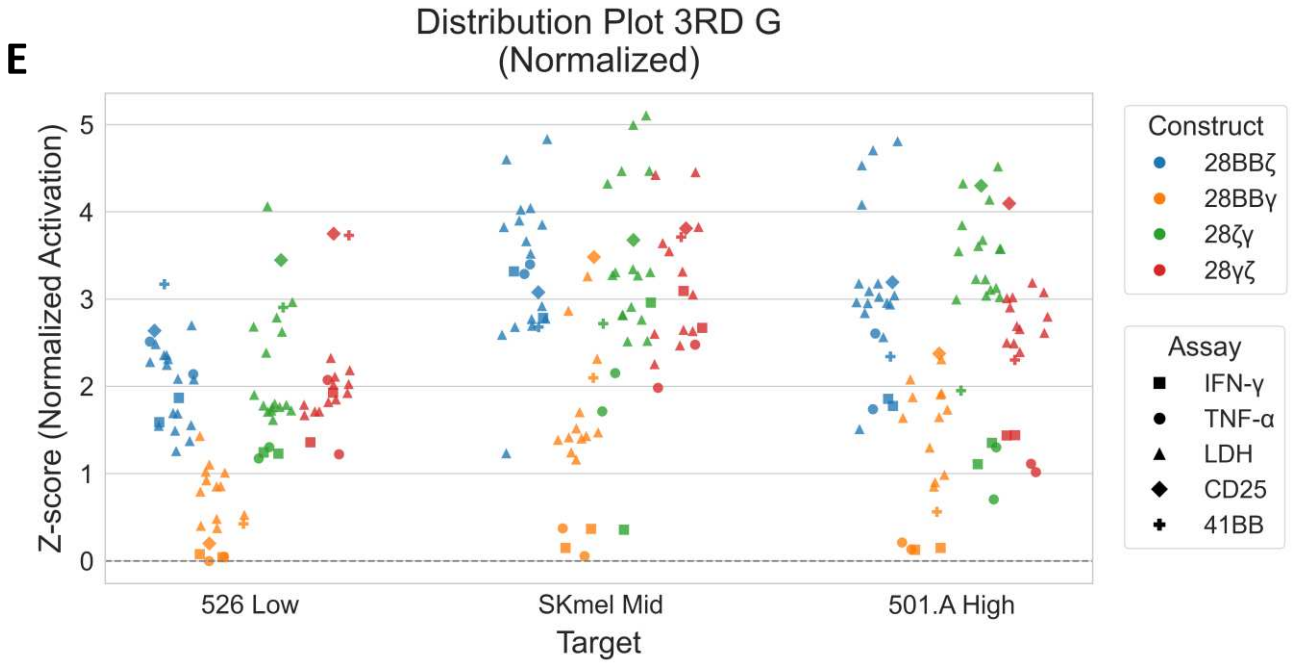
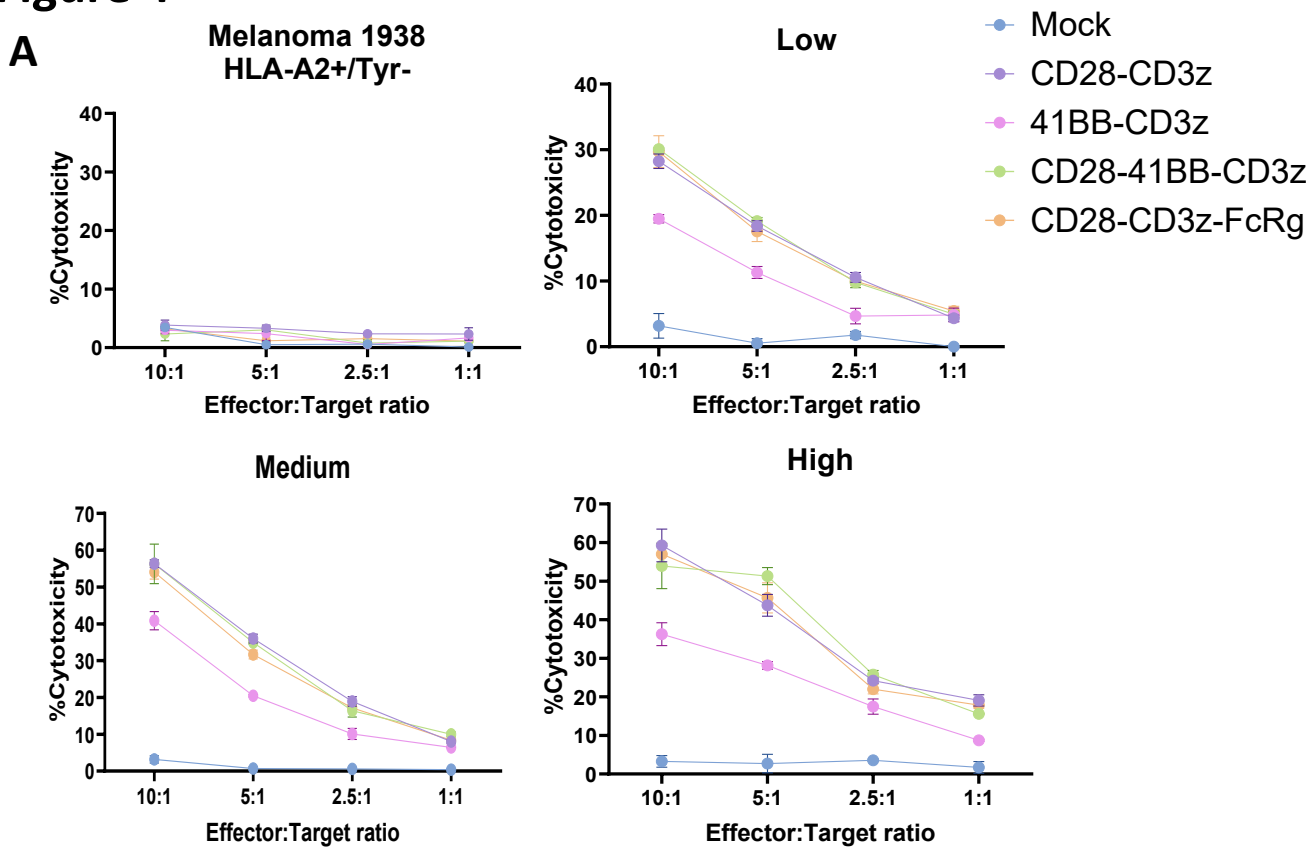
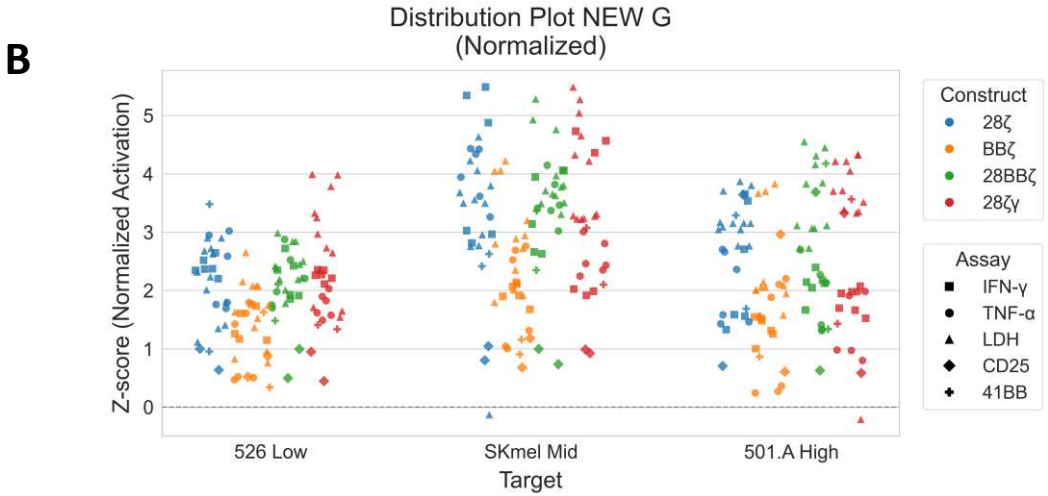
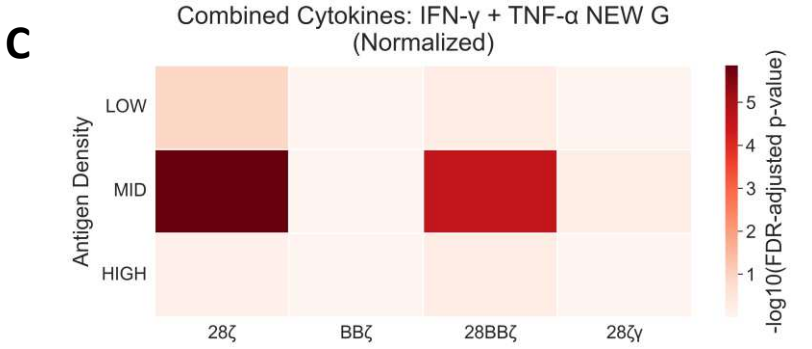
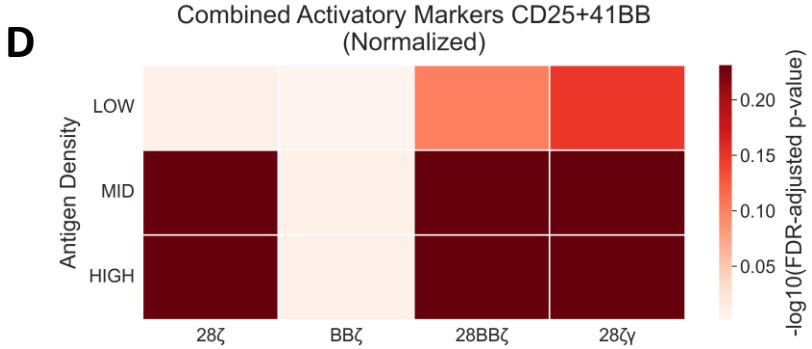

E
Distribution Plot 3RD G
(Normalized)
Z-score (Normalized Activation)
526 Low
SKmel Mid
501.A High
Target
Construct
28BBζ
28BBγ
28ζγ
28γζ
Assay
IFN-γ
TNF-α
LDH
CD25
41BB

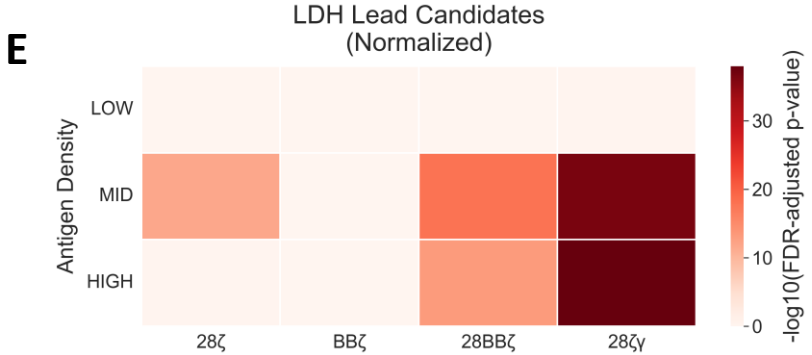
Figure 4


A
Melanoma 1938
HLA-A2+/Tyr-
Low
Medium
High
Mock
CD28-CD3z
41BB-CD3z
CD28-41BB-CD3z
CD28-CD3z-FcRg
%Cytotoxicity
Effector:Target ratio
10:1
5:1
2.5:1
1:1


B
Distribution Plot NEW G
(Normalized)
Z-score (Normalized Activation)
526 Low
SKmel Mid
501.A High
Target
Construct
28ζ
BBζ
28BBζ
28ζγ
Assay
IFN-γ
TNF-α
LDH
CD25
41BB


C
Combined Cytokines: IFN-γ + TNF-α NEW G
(Normalized)
Antigen Density
LOW
MID
HIGH
28ζ
BBζ
28BBζ
28ζγ
-log10(FDR-adjusted p-value)


D
Combined Activatory Markers CD25+41BB
(Normalized)
Antigen Density
LOW
MID
HIGH
28ζ
BBζ
28BBζ
28ζγ
-log10(FDR-adjusted p-value)


E
LDH Lead Candidates
(Normalized)
Antigen Density
LOW
MID
HIGH
28ζ
BBζ
28BBζ
28ζγ
-log10(FDR-adjusted p-value)

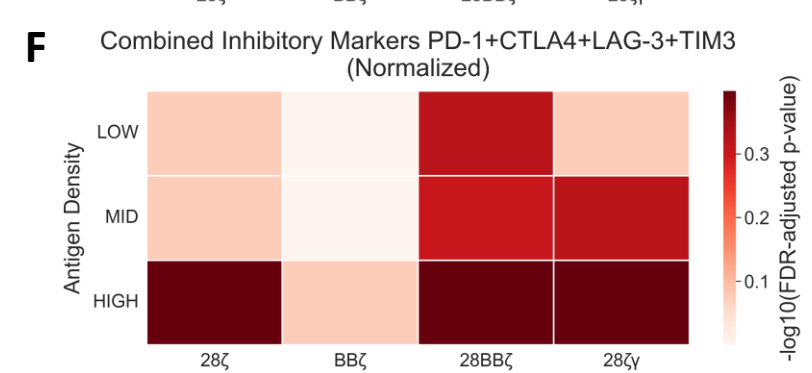
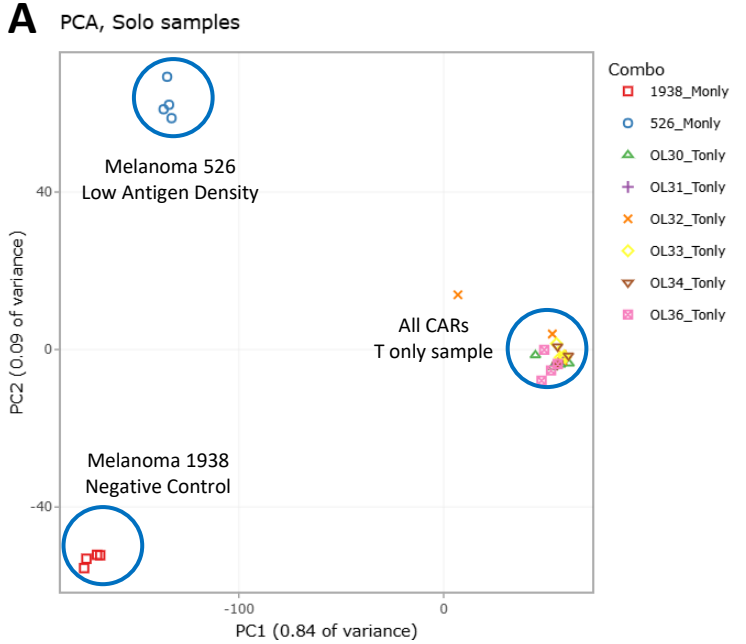
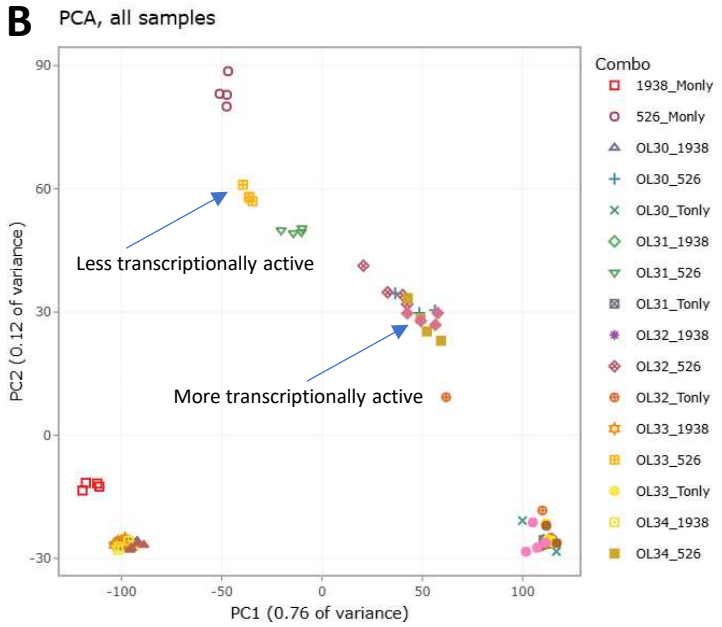
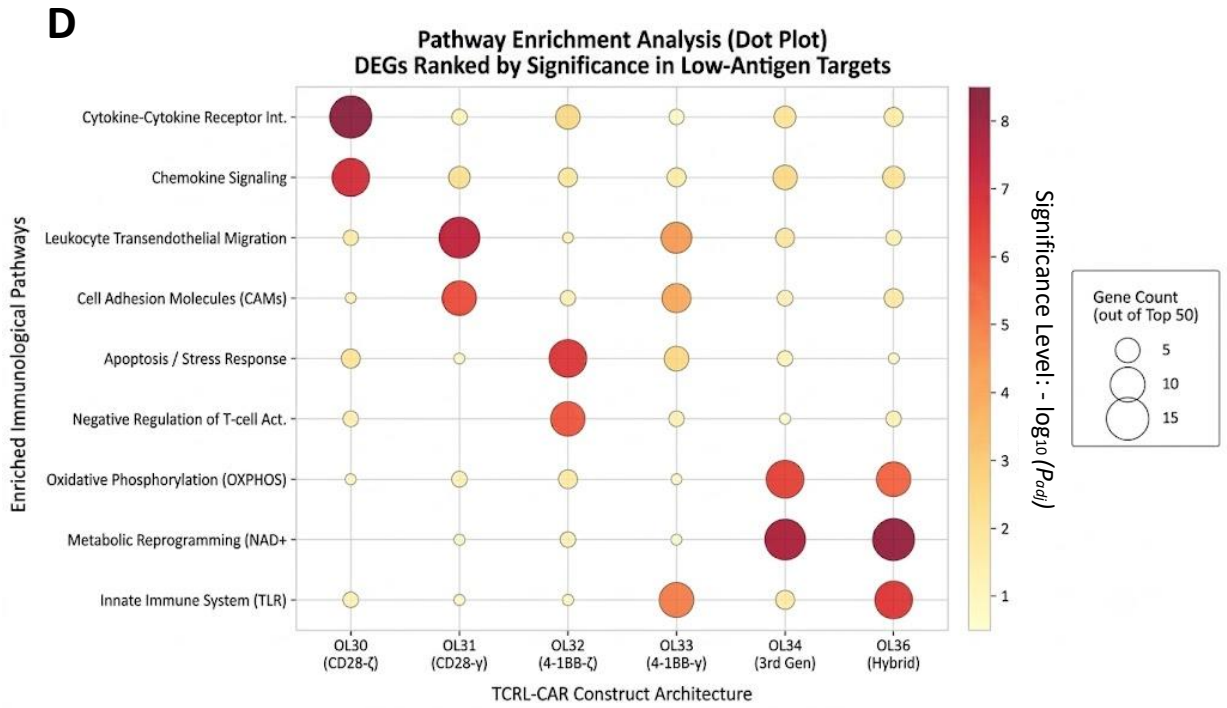
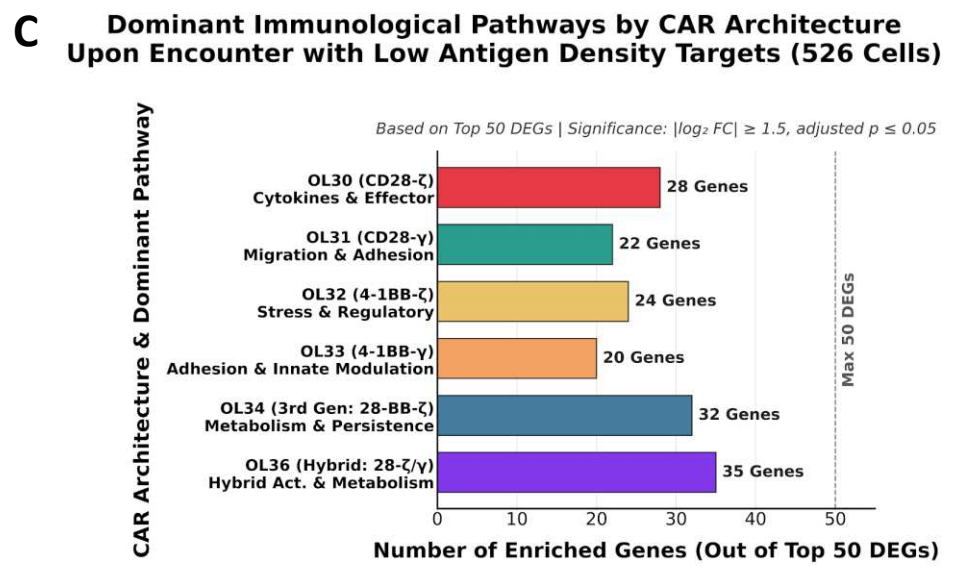

F
Combined Inhibitory Markers PD-1+CTLA4+LAG-3+TIM3
(Normalized)
Antigen Density
LOW
MID
HIGH
28ζ
BBζ
28BBζ
28ζγ
-log10(FDR-adjusted p-value)

Figure 5


A
PCA, Solo samples
Melanoma 526
Low Antigen Density
All CARs
T only sample
Melanoma 1938
Negative Control
PC2 (0.09 of variance)
PC1 (0.84 of variance)
Combo
1938_Monly
526_Monly
OL30_Tonly
OL31_Tonly
OL32_Tonly
OL33_Tonly
OL34_Tonly
OL36_Tonly


B
PCA, all samples
Less transcriptionally active
More transcriptionally active
PC2 (0.12 of variance)
PC1 (0.76 of variance)
Combo
1938_Monly
526_Monly
OL30_1938
OL30_526
OL30_Tonly
OL31_1938
OL31_526
OL31_Tonly
OL32_1938
OL32_526
OL32_Tonly
OL33_1938
OL33_526
OL33_Tonly
OL34_1938
OL34_526


D
Pathway Enrichment Analysis (Dot Plot)
DEGs Ranked by Significance in Low-Antigen Targets
Cytokine-Cytokine Receptor Int.
Chemokine Signaling
Leukocyte Transendothelial Migration
Cell Adhesion Molecules (CAMs)
Apoptosis / Stress Response
Negative Regulation of T-cell Act.
Oxidative Phosphorylation (OXPHOS)
Metabolic Reprogramming (NAD+
Innate Immune System (TLR)
Enriched Immunological Pathways
OL30 (CD28-ζ)
OL31 (CD28-γ)
OL32 (4-1BB-ζ)
OL33 (4-1BB-γ)
OL34 (3rd Gen)
OL36 (Hybrid)
TCRL-CAR Construct Architecture
Significance Level: - log10 (Padj)
Gene Count (out of Top 50)
5
10
15


C
Dominant Immunological Pathways by CAR Architecture
Upon Encounter with Low Antigen Density Targets (526 Cells)
Based on Top 50 DEGs | Significance: |log2 FC| ≥ 1.5, adjusted p ≤ 0.05
CAR Architecture & Dominant Pathway
OL30 (CD28-ζ)
Cytokines & Effector
28 Genes
OL31 (CD28-γ)
Migration & Adhesion
22 Genes
OL32 (4-1BB-ζ)
Stress & Regulatory
24 Genes
OL33 (4-1BB-γ)
Adhesion & Innate Modulation
20 Genes
OL34 (3rd Gen: 28-BB-ζ)
Metabolism & Persistence
32 Genes
OL36 (Hybrid: 28-ζ/γ)
Hybrid Act. & Metabolism
35 Genes
Max 50 DEGs
Number of Enriched Genes (Out of Top 50 DEGs)

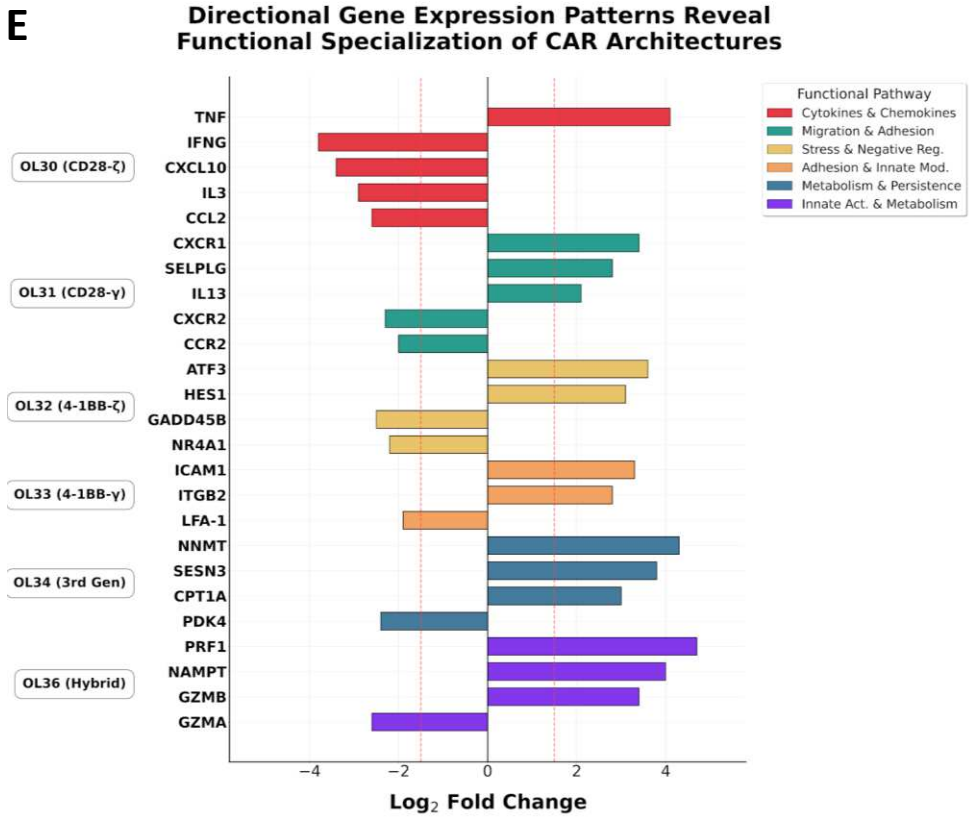
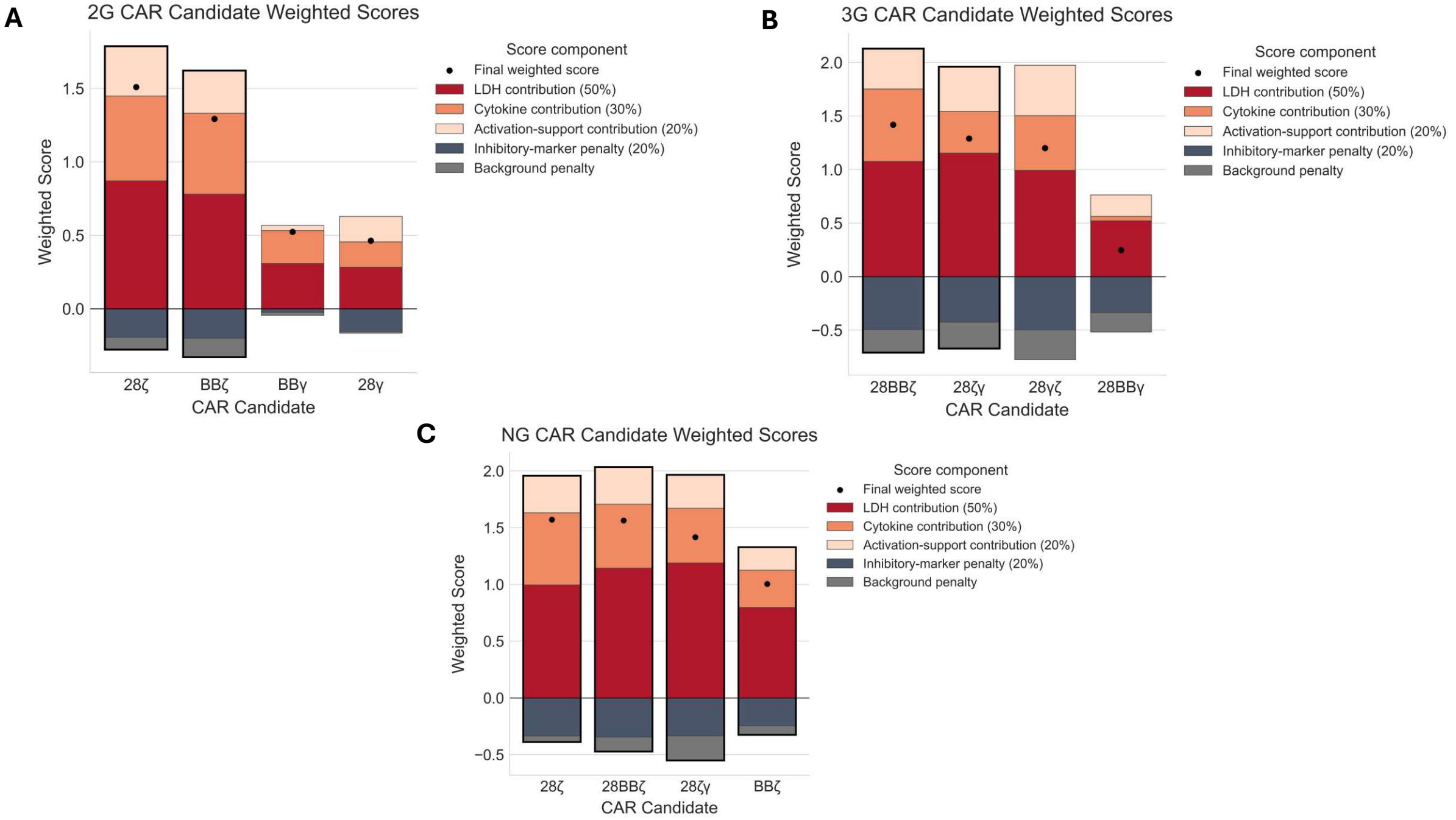

E
Directional Gene Expression Patterns Reveal
Functional Specialization of CAR Architectures
Functional Pathway
Cytokines & Chemokines
Migration & Adhesion
Stress & Negative Reg.
Adhesion & Innate Mod.
Metabolism & Persistence
Innate Act. & Metabolism
OL30 (CD28-ζ)
OL31 (CD28-γ)
OL32 (4-1BB-ζ)
OL33 (4-1BB-γ)
OL34 (3rd Gen)
OL36 (Hybrid)
TNF
IFNG
CXCL10
IL3
CCL2
CXCR1
SELPLG
IL13
CXCR2
CCR2
ATF3
HES1
GADD45B
NR4A1
ICAM1
ITGB2
LFA-1
NNMT
SESN3
CPT1A
PDK4
PRF1
NAMPT
GZMB
GZMA
Log2 Fold Change

Figure 6


A
2G CAR Candidate Weighted Scores
Weighted Score
1.5
1.0
0.5
0.0
28ζ
BBζ
BBγ
28γ
CAR Candidate
Score component
Final weighted score
LDH contribution (50%)
Cytokine contribution (30%)
Activation-support contribution (20%)
Inhibitory-marker penalty (20%)
Background penalty
B
3G CAR Candidate Weighted Scores
Weighted Score
2.0
1.5
1.0
0.5
0.0
−0.5
28BBζ
28ζγ
28γζ
28BBγ
CAR Candidate
Score component
Final weighted score
LDH contribution (50%)
Cytokine contribution (30%)
Activation-support contribution (20%)
Inhibitory-marker penalty (20%)
Background penalty
C
NG CAR Candidate Weighted Scores
Weighted Score
2.0
1.5
1.0
0.5
0.0
−0.5
28ζ
28BBζ
28ζγ
BBζ
CAR Candidate
Score component
Final weighted score
LDH contribution (50%)
Cytokine contribution (30%)
Activation-support contribution (20%)
Inhibitory-marker penalty (20%)
Background penalty

Supplementary Files

This is a list of supplementary files associated with this preprint. Click to download.

- SupplementaryFigureS1.pdf
- SupplementaryFigureS2.pdf
- SupplementaryFigureS3.pdf
- SupplementaryTableT1.pdf